Electronic Supplementary Material (ESI) for Journal of Materials Chemistry C.

Minimizing geminate recombination losses in small-molecule-based organic solar cells

Rafael Sandoval-Torrientes,[1] Alexey Gavrik,[1,2] Anna Isakova,[1] Abasi Abudulimu,[1] Joaquín Calbo,[3] Juan Aragó,[3] José Santos,[1,4] Enrique Ortí,[3] Nazario Martín,*[1,4] Vladimir Dyakonov,*[2] Larry Lüer*[1]*

[1] IMDEA Nanociencia, Campus Universitario de Cantoblanco, 28049, Madrid, Spain. E-mail: larry.luer@imdea.org

[2] Experimental Physics VI, University of Würzburg, 97074, Germany

[3] Instituto de Ciencia Molecular, Universidad de Valencia, Paterna, 46980, Spain. E-mail: enrique.orti@uv.es

[4] Facultad de Ciencias Químicas, Universidad Complutense de Madrid, Madrid, 28040, Spain. E-mail: nazmar@ucm.es

Supporting information

Table of contents

1. Experimental section

General Methods. Chemicals and reagents were purchased from commercial suppliers and used as received. All solvents were dried according to standard procedures. Air-sensitive reactions were carried out under nitrogen atmosphere. The device preparation was done in a glovebox under nitrogen atmosphere. Flash chromatography was performed using silica gel (Fluorochem, Silicagel 60A, 40-63 micron). Analytical thin-layer chromatography (TLC) was performed using aluminum-coated Merck Kieselgel 60 F254 plates. NMR spectra were recorded on a Bruker Advance 300 (^{1}H: 400 MHz; ^{13}C: 101 MHz) spectrometer at 298 K using partially deuterated solvents as internal standards. Coupling constants (*J*) are denoted in Hz and chemical shifts (δ) in ppm. Multiplicities are denoted as follows: s = singlet, d = doublet, t = triplet, m = multiplet. UV-vis spectra were recorded in a Varian Cary 50 spectrophotometer. FT-IR spectra were recorded on a Bruker Tensor 27 (ATR device) spectrometer. Mass spectra matrix-assisted laser desorption ionization (coupled to a Time-of-Flight analyzer) experiments (MALDI-TOF) were recorded on a MAT 95 thermo spectrometer and a Bruker REFLEX spectrometer respectively. Thermogravimetric analysis (TGA) was performed using a TA Instruments TGAQ500 with a ramp of 10 °C/min under N_2 from 100 to 1000 °C. Differential scanning calorimetry (DSC) was run on a Discovery DSC from TA instruments. Three cycles were recorded under nitrogen, heating (until 400 °C) and cooling (50 °C) at 20 °C/min of scanning rate. Cyclic voltammetry (CV) experiments were performed in 0.1 M Bu_4NPF_6 DCM solution. Glassy carbon was used as a working electrode and platinum wires as counter and reference electrodes. Before each measurement, solutions were deoxygenated with N_2. Ferrocene was added as an internal standard; its oxidation potential in DCM was set at 0.7 V *vs.* normal hydrogen electrode (NHE) and materials' oxidation potential were recalculated in reference to NHE. Elemental analysis was performed employing a LECO CHNS-932 elemental analyser.

2. Synthetic details and characterization

Compounds **1**,[1] **3**,[2] **4**,[3] **5**[4] and **10**[5] were synthesized following previously reported procedures. Compound **2** was purchased from a commercial chemical supplier.

3,6-Bis(4-(diphenylamino)phenyl)-9H-fluoren-9-one (6). Into a 100 mL 2-neck round flask filled with dry DMF (20 mL) and nitrogen, **1** (300 mg, 0.88 mmol), (4-(diphenylamino)phenyl)boronic acid (**2**) (540 mg, 1.86 mmol) and $Pd(PPh_3)_4$ (101 mg, 0.09 mmol) were added. The mixture was degassed for 30 minutes. Then, K_3PO_4 (3.00 g, 14.0 mmol) was added in one portion. The resulting mixture was stirred at 90 °C for 6 h. The mixture was cooled to room temperature and washed with H_2O (30 mL). After extraction with DCM (3 × 15 mL), combined organic extracts were dried over anhydrous Na_2SO_4, filtered, and evaporated. The resulting crude was purified by flash chromatography (silica gel, hexane/DCM 1:4) yielding an orange solid (480 mg, 80%). ^{1}H NMR (400 MHz, THF- d^8) δ: 8.01 (s, 2H), 7.67–7.61 (m, 6H), 7.57 (dd, *J* = 7.8, 1.4 Hz, 2H), 7.29–7.23 (m, 8H), 7.16–7.09 (m, 12H), 7.05–7.00 (m, 4H) ppm. ^{13}C NMR (101 MHz, THF-d^8) δ: 192.4, 149.6, 148.7, 148.0, 146.1, 134.9, 134.3, 130.3, 128.9, 128.0, 126.1, 125.7, 125.1, 124.4, 119.6 ppm. HRMS (MALDI-TOF): *m/z* calculated for $C_{49}H_{34}N_2O_1$: 666.2666, found: 666.2694.

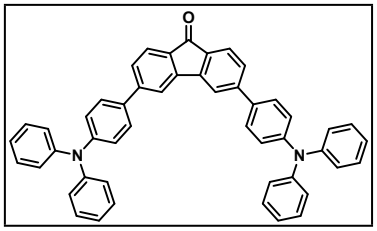

3,6-bis(4-(di-p-tolylamino)phenyl)-9H-fluoren-9-one (7). Into a 100mL 2-neck round flask filled with dry DMF (20 mL) and nitrogen, **1** (338 mg, 1.00 mmol), 4-methyl-*N*-(4-(4,4,5,5-tetramethyl-1,3,2-dioxaborolan-2-yl)phenyl)-*N*-(*p*-tolyl)aniline (**3**) (800 mg, 2.00 mmol) and $Pd(PPh_3)_4$ (115 mg, 0.10 mmol) were added. The mixture was degassed for 30 minutes. Then, K_3PO_4 (3.00 g, 14.0 mmol) was added in one portion. The resulting mixture was stirred at 90 °C for 6 h. The mixture was cooled to room temperature and washed with H_2O (30 mL). After extraction with DCM (3 × 15 mL), combined organic extracts were dried over anhydrous Na_2SO_4, filtered, and evaporated. The resulting crude was purified by flash chromatography (silica gel, hexane/DCM 1:8) yielding a light orange solid (615 mg, 85%). ^{1}H NMR (400 MHz, THF-d^8) δ: 8.01 (d, *J* = 2H, 1.2 Hz), 7.66–7.59 (m, 6H), 7.56 (dd, *J* = 7.8, 1.2 Hz, 2H), 7.29–7.05 (m, 12H), 7.04–6.97 (m, 8H), 2.30 (s, 12H) ppm. ^{13}C NMR (101 MHz, THF-d^8) δ: 192.4, 149.9, 148.1, 146.2, 146.1, 134.1,

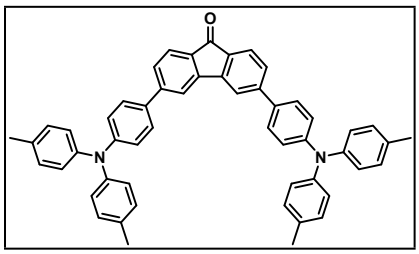

134.0, 133.8, 130.9, 128.8, 127.8, 125.9, 125.0, 123.1, 119.4, 21.0 ppm. HRMS (MALDI-TOF): *m/z* calculated for $C_{53}H_{42}N_2O_1$: 722.3292, found: 722.3289.

3,6-bis(4-(bis(4-methoxyphenyl)amino)phenyl)-9H-fluoren-9-one (8). Into a 100mL 2-neck round flask filled with dry DMF (20 mL) and nitrogen, **1** (300 mg, 0.88 mmol), 4 methoxy-*N*-(4-methoxyphenyl)-*N*-(4-(4,4,5,5-tetramethyl-1,3,2-dioxaborolan-2-yl)phenyl)aniline (**4**) (650 mg, 1.86 mmol) and $Pd(PPh_3)_4$ (101 mg, 0.09 mmol) were added. The mixture was degassed for 30 minutes. Then, K_3PO_4 (3.00 g, 14.0 mmol) was added in one portion. The resulting mixture was stirred at 90 °C for 6 h. The mixture was cooled to room temperature and washed with H_2O (30 mL). After extraction with DCM (3×15 mL), combined organic extracts were dried over anhydrous Na_2SO_4, filtered, and evaporated. The resulting crude was purified by flash chromatography (silica gel, hexane/DCM 1:8) yielding a red-orange solid (590 mg, 85%). ^{1}H NMR (400 MHz, $CDCl_3$) δ: 7.73 (s, 2H), 7.68 (d, *J* = 7.7 Hz, 2H), 7.46 (d, *J* = 7.3 Hz, 6H), 7.03–6.92 (m, 12H), 6.87 (d, *J* = 7.8 Hz, 8H), 3.82 (s, 12H) ppm. ^{13}C NMR (101 MHz, $CDCl_3$) δ: 193.0, 156.2, 149.2, 147.3, 144.9, 140.4, 132.9, 131.5, 127.7, 126.9, 126.8, 124.6, 120.1, 118.1, 114.8, 55.5 ppm. HRMS (MALDI-TOF): *m/z* calculated for $C_{53}H_{42}N_2O_5$: 786.3088, found: 786.3089.

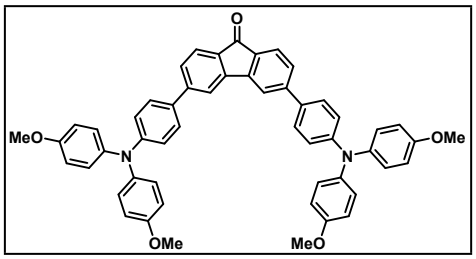

3,6-bis(bis(4-methoxyphenyl)amino)-9H-fluoren-9-one (9). A solution of **42** (192 mg, 0.57 mmol), **61** (288 mg, 1.27 mmol), $Pd_2(dba)_3$ (21 mg, 0.02 mmol) and XPhos (33.0 mg, 0.06 mmol) in dry toluene (20 mL) was deaerated by bubbling nitrogen during 30 min. Then NaO^tBu (165 mg, 1.72 mmol) was added in one portion and the resulting mixture was stirred at 110 °C for 18 h. Upon cooling to room temperature, the mixture was quenched with H_2O (20 mL) and extracted with $CHCl_3$ (3 × 15 mL). Combined organic extracts were dried over anhydrous Na_2SO_4, filtered, and evaporated. The product was purified by flash chromatography (silica gel, hexane/DCM 1:1) yielding a red-orange powder (272 mg, 75%). ^{1}H NMR (400 MHz, THF-d^8) δ: 7.29 (d, *J* = 8.2 Hz, 2H), 7.07–7.01 (m, 8H), 6.91 (d, *J* = 2.1 Hz, 2H), 6.88–6.83 (m, 8H), 6.59 (dd, *J* = 8.2, 2.0 Hz, 2H), 3.75 (s, 12H) ppm. ^{13}C NMR (101 MHz, THF-

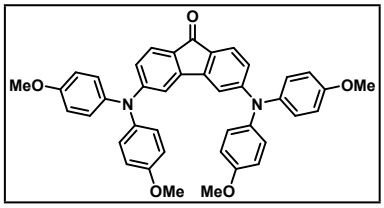

d[8]) δ: 189.9, 158.2, 155.1, 146.2, 140.9, 128.3, 125.2, 120.6, 119.3, 115.8, 111.6, 55.8 ppm. HRMS (MALDI-TOF): *m/z* calculated for $C_{41}H_{34}N_2O_5$: 634.7191, found: 634.7194.

Compound M0. Compounds **9** (272 mg, 0.43 mmol), rhodanine **10** (105 mg, 0.42 mmol), and β-alanine (38.0 mg, 0.42 mmol) were dissolved in a mixture of glacial acetic acid (10 mL) and toluene (10mL) and stirred at 118 °C for 18 h. Upon cooling to room temperature, the mixture was diluted with water (100 mL) and extracted with $CHCl_3$ (3 ×15 mL), the organic extracts were washed with $NaHCO_3$ saturated solution until no gas development was observed, dried over anhydrous Na_2SO_4, filtered, and evaporated. The remaining residue was purified by flash chromatography (silica gel, hexane/ethyl acetate 4:1), giving a dark brown solid (90 mg, 24%). ^{1}H NMR (400 MHz, acetone-d[6]) δ: 9.11 (d, *J* = 8.9 Hz, 1H), 7.60 (d, *J* = 8.8 Hz, 1H), 7.14–7.08 (m, 8H), 6.94–6.90 (m, 9H), 6.88 (d, *J* = 2.4 Hz, 1H), 6.66 (dd, *J* = 8.8, 2.4 Hz, 1H), 6.59 (dd, *J* = 8.9, 2.4 Hz, 1H), 4.05 (d, *J* = 7.4 Hz, 2H), 3.81 (s, 12H), 2.16–2.07 (m, 1H), 1.41–1.30 (m, 8H), 0.92 (t, *J* = 7.4 Hz, 3H), 0.87 (t, *J* = 7.1 Hz, 3H) ppm. ^{13}C NMR (101 MHz, acetone-d[6]) δ: 192.6, 167.3, 158.2, 158.1, 152.7, 152.5, 144.5, 144.3, 142.6, 140.3, 140.1, 131.8, 130.3, 129.2, 128.9, 128.7, 128.6, 117.8, 117.7, 115.8, 115.8, 110.4, 110.1, 55.8, 49.1, 37.9, 31.4, 24.8, 23.7, 14.3, 11.0 ppm. HRMS (MALDI-TOF): *m/z* calculated for $C_{52}H_{51}N_3O_5S_2$: 861.3265, found: 861.3264. FTIR (neat): 2955, 2929, 2856, 2834, 1691, 1599, 1559, 1504, 1484, 1453, 1393, 1354, 1330, 1275, 1241, 1184, 1130, 1070, 1035, 828 cm^{-1}. Anal. calc: C, 72.45; H, 5.96; N, 4.87; S, 7.44, found: C, 72.47; H, 5.84; N, 4.91; S, 8.31.

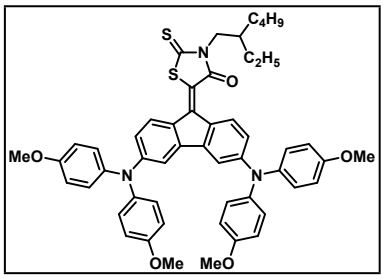

Compound M1. Compounds **6** (300 mg, 0.45 mmol), rhodanine **10** (165 mg, 0.67 mmol) and β-alanine (80.0 mg, 0.90 mmol) were dissolved in a mixture of glacial acetic acid (10 mL) and toluene (10 mL) and stirred at 118 °C for 18 h. Upon cooling to room temperature, the mixture was diluted with water (100 mL) and extracted with $CHCl_3$ (3 × 15 mL), the organic extracts were washed with $NaHCO_3$ saturated solution until no gas development was observed, dried over anhydrous Na_2SO_4, filtered, and evaporated. The remaining residue was purified by flash chromatography (silica gel,

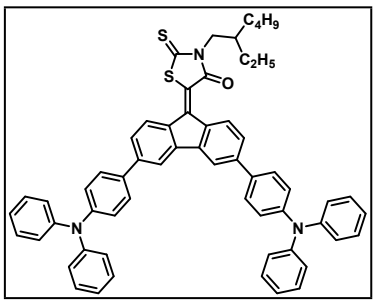

hexane/DCM 1:4), giving a red-brown solid (141 mg, 35%). ^{1}H NMR (400 MHz, acetone-d^{6}) δ: 9.18 (d, *J* = 8.4 Hz, 1H), 8.05 (d, *J* = 1.5 Hz, 1H), 8.03 (d, *J* = 1.3 Hz, 1H), 7.70–7.61 (m, 5H), 7.51 (d, *J* = 8.4, 1.5 Hz, 1H), 7.45 (dd, *J* = 8.5, 1.5 Hz, 1H), 7.37–7.28 (m, 8H), 7.15–7.04 (m, 16H), 4.00 (d, *J* = 7.4 Hz, 2H), 2.14–2.09 (m, 1H), 1.42–1.24 (m, 8H), 0.93 (t, *J* = 7.4 Hz, 3H), 0.88 (t, *J* = 6.9 Hz, 3H) ppm. ^{13}C NMR (101 MHz, THF-d^{8}) δ: 192.9, 167.9, 149.4, 149.3, 148.8, 148.7, 144.5, 144.3, 143.9, 141.4, 137.8, 135.9, 135.0, 134.6, 131.2, 130.3, 130.3, 128.9, 128.7, 127.1, 126.8, 125.7, 125.6, 124.5, 124.4, 124.3, 124.2, 123.6, 119.3, 118.7, 49.5, 38.4, 31.7, 29.6, 24.1, 14.6, 11.2 ppm. HRMS (MALDI-TOF): *m/z* calculated for $C_{60}H_{51}N_3OS_2$: 893.3488, found: 893.3468. FTIR (neat): 3035, 2957, 2926, 2857, 1701, 1591, 1530, 1514, 1492, 1444, 1392, 1329, 1313, 1280, 1196, 1179, 1135, 1075, 1027, 876, 822, 753, 696, 620 cm^{-1}. Anal. calc: C, 80.59; H, 5.75; N, 4.70; S, 7.17, found: C, 80.51; H, 5.69; N, 4.91; S, 7.71.

Compound M2. Compounds **7** (470 mg, 0.65 mmol), rhodanine **10** (240 mg, 0.98 mmol),

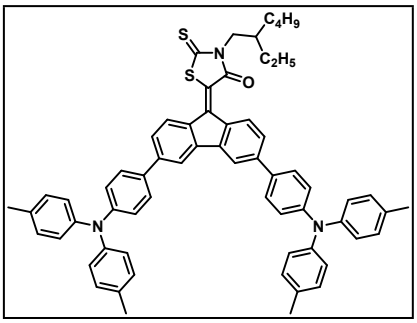

β-alanine (110 mg, 1.31 mmol) were dissolved in a mixture of glacial acetic acid (10 mL) and toluene (10 mL) and stirred at 118 °C for 18 h. Upon cooling to room temperature, the mixture was diluted with water (100 mL) and extracted with $CHCl_3$ (3 × 15 mL), the organic extracts were washed with $NaHCO_3$ saturated solution until no gas development was observed, dried over anhydrous Na_2SO_4, filtered, and evaporated. The remaining residue was purified by flash chromatography (silica gel, hexane/toluene 1:3), giving a dark brown solid (250 mg, 40%). ^{1}H NMR (400 MHz, THF-d^{8}) δ: 9.39 (d, *J* = 8.5 Hz, 1H), 8.10 (d, *J* = 1.6 Hz, 1H), 8.07 (d, *J* = 1.7 Hz, 1H), 7.90 (d, *J* = 8.3 Hz, 1H), 7.66–7.62 (m, 4H), 7.60 (dd, *J* = 8.3, 1.8 Hz, 1H), 7.54 (dd, *J* = 8.5, 1.9 Hz, 1H), 7.07 (dd, *J* = 12.0, 5.1 Hz, 12H), 7.03–6.99 (m, 8H), 4.11 (d, *J* = 7.3 Hz, 2H), 2.30 (s, 12H), 2.20–2.10 (m, 1H), 1.46–1.28 (m, 8H), 0.95 (t, *J* = 7.4 Hz, 3H), 0.91 (t, *J* = 7.1 Hz, 3H) ppm. ^{13}C NMR (101 MHz, THF-d^{8}) δ: 192.9, 167.8, 149.7, 149.6, 146.3, 146.2, 144.6, 144.4, 144.3, 143.9, 141.5, 137.6, 135.7, 134.0, 133.9, 133.8, 133.6, 130.9, 128.6, 128.5, 126.6, 125.9, 125.9, 123.3, 123.2, 119.1, 118.6, 49.5, 38.4, 31.7, 29.6, 24.1, 21.1, 14.6, 11.2 ppm. HRMS (MALDI-TOF): *m/z* calculated for $C_{64}H_{59}N_3OS_2$:949.4094, found: 949.4078. FTIR (neat): 3026, 2956, 2922, 2857, 1701,

1597, 1529, 1506, 1478.56, 1445, 1392, 1320, 1292, 1277, 1195, 1134, 1074, 1020, 876, 814, 766, 737 cm^{-1}. Anal. calc: C, 80.89; H, 6.26; N, 4.42; S, 6.75, found: C, 80.85; H, 6.33; N, 4.49; S, 6.69.

Compound M3. Compounds **8** (410 mg, 0.52 mmol), rhodanine **10** (190 mg, 0.78 mmol),

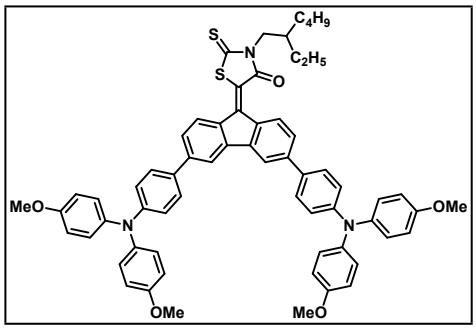

β-alanine (93.0 mg, 1.04 mmol) were dissolved in a mixture of glacial acetic acid (10 mL) and toluene (10 mL) and stirred at 118 °C for 18 h. Upon cooling to room temperature, the mixture was diluted with water (100 mL) and extracted with $CHCl_3$ (3 × 15 mL), the organic extracts were washed with $NaHCO_3$ saturated solution until no gas development was observed, dried over anhydrous Na_2SO_4, filtered, and evaporated. The remaining residue was purified by flash chromatography (silica gel, hexane/DCM 1:4), giving a dark brown solid (100 mg, 20%). ^{1}H NMR (400 MHz, acetone-d^6) δ: 9.01 (d, *J* = 8.4 Hz, 1H), 7.76 (d, *J* = 1.2 Hz, 1H), 7.74 (d, *J* = 1.4 Hz, 1H), 7.50–7.41 (m, 4H), 7.39 (d, *J* = 8.3 Hz, 1H), 7.28 (dd, *J* = 8.3, 1.6 Hz, 1H), 7.24 (dd, *J* = 8.5, 1.7 Hz, 1H), 7.06–7.01 (m, 8H), 6.94–6.88 (m, 8H), 6.85 (t, *J* = 8.6 Hz, 4H), 3.89 (d, *J* = 7.5 Hz, 2H), 3.79 (s, *J* = 1.3 Hz, 12H), 2.09–2.07 (m, 1H), 1.38–1.26 (m, 8H), 0.90 (t, *J* = 7.3 Hz, 3H), 0.86 (t, *J* = 6.9 Hz, 3H) ppm. ^{13}C NMR (101 MHz, acetone-d^6) δ: 192.5, 167.0, 157.4, 157.4, 149.8, 149.7, 143.8, 143.7, 143.5, 143.4, 141.6, 141.2, 141.1, 136.8, 134.9, 132.0, 131.5, 130.8, 128.4, 128.3, 127.9, 127.9, 126.2, 125.8, 121.9, 120.3, 120.2, 118.4, 117.9, 115.7, 55.8, 49.3, 38.0, 31.4, 24.8, 23.8, 14.4, 11.1 ppm. HRMS (MALDI-TOF): *m/z* calculated for $C_{64}H_{59}N_3O_5S_2$: 1013.3903, found: 1013.3891. FTIR (neat): 3037, 2996, 2953, 2928, 2855, 2833, 1670, 1597, 1505, 1479, 1463, 1443, 1392, 1318, 1281, 1240, 1195, 1134, 1106, 1074, 1035, 976, 876, 824, 781, 766, 728, 597, 578 cm^{-1}. Anal. calc: C, 75.79; H, 5.86; N, 4.14; S, 6.32, found: C, 75.83; H, 5.84; N, 4.17; S, 6.34.

3. Electrochemical Properties

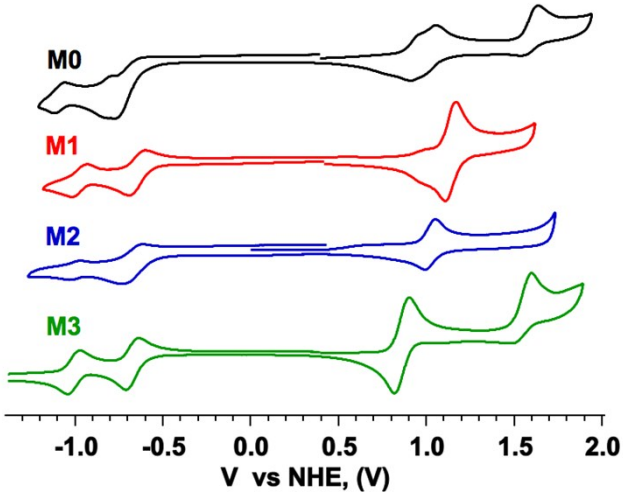

Fig. S1 Cyclic voltammograms of dyes **M0**–**3** recorded in a deaerated DCM solution containing 0.1 M Bu_4NPF_6 as supporting electrolyte, glassy carbon working electrode and Pt wires as counter and reference electrodes were employed. Fc/Fc^+ internal standard was employed and all potentials accordingly referenced against normalized hydrogen electrode (NHE).

Table S1 Cyclic voltammetry electrochemical data and HOMO/LUMO energies of the **M0**–**3** dyes.

Compound	$E_{1/2}^{ox}$ [V]	$E_{1/2}^{red}$ [V]	E_{gap}^{cv} [V][a]	E_{HOMO}/E_{LUMO} [eV][b]
M0	0.96	-0.80	1.76	−5.36/−3.60
M1	1.16	-0.67	1.83	−5.56/−3.73
M2	1.02	-0.71	1.73	−5.42/−3.69
M3	0.90	-0.69	1.59	−5.30/−3.71

[a] Calculated as $E_{gap}^{cv} = E_{1/2}^{ox} - E_{1/2}^{red}$; [b] calculated as $E_{HOMO} = -[E_{1/2}^{ox} + 4.4]$ eV; $E_{LUMO} = E_{HOMO} + E_{gap}^{cv}$.

4. Theoretical and Computational Details

4.1. Geometrical Optimization

Minimum-energy geometries of the **M0**–**3** dyes were calculated under the density functional theory (DFT) framework using the standard and popular hybrid exchange-

correlation B3LYP functional and the correlation-consistent cc-pVDZ basis set.[6,7] Fig. S2 displays the optimized geometry for the representative **M2** and **M0** derivatives. Theoretical calculations predict for all the four molecules a planar fluorene–rhodanine core with short O···H and S···H distances calculated around 2.0 and 2.4 Å, respectively. The triphenylamine (TPA) substituents are slightly distorted from planarity due to the evident steric hindrance between vicinal H atoms, with short H···H contacts calculated at *ca.* 3.1 Å. Similarly, TPA moieties alleviate steric congestion with fluorene core in **M1**, **M2** and **M3** by tilting from planarity with a dihedral angle of 33° (Fig. S2a). Peripheral substitution of the TPA donor moieties (R = H, –OMe, –Me) is calculated to have a negligible impact on the minimum-energy geometry parameters.

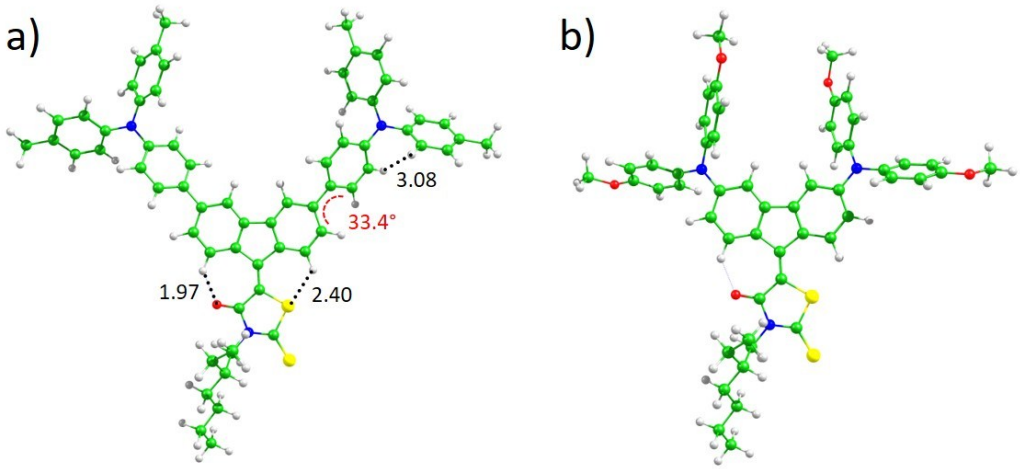

Fig. S2 Minimum-energy structures calculated for representative **M2** (a) and **M0** (b) rhodanine-based derivatives.

4.2. Molecular Orbital Analysis

Fig. S3 displays the frontier molecular orbital energies for the rhodanine-based derivatives. As expected, the highest-occupied molecular orbital (HOMO) and HOMO–1 are localized over the two electron-donor TPA moieties in **M1**, **M2** and **M3**. Otherwise, the HOMO–2 spreads over the rhodanine and part of the fluorene fragments, and the HOMO–3 is centred on the fluorene core (Fig. S3). On the other hand, the lowest-unoccupied molecular orbital (LUMO) and LUMO+1 are localized over the fluorene-rhodanine core, whereas the LUMO+2 and LUMO+3 mainly involve the fluorene core and one TPA unit. Theoretical calculations predict an increase in the HOMO energy upon inclusion of stronger electron-donor groups, going from **M1** (–H) to **M2** (–Me) and to

M3 (–OMe) with values of –5.19 to –5.04 and to –4.84 eV, respectively. The same trend but less pronounced is predicted for the LUMO energy, which increases from –2.93 to –2.77 eV in going from **M1** to **M3**.

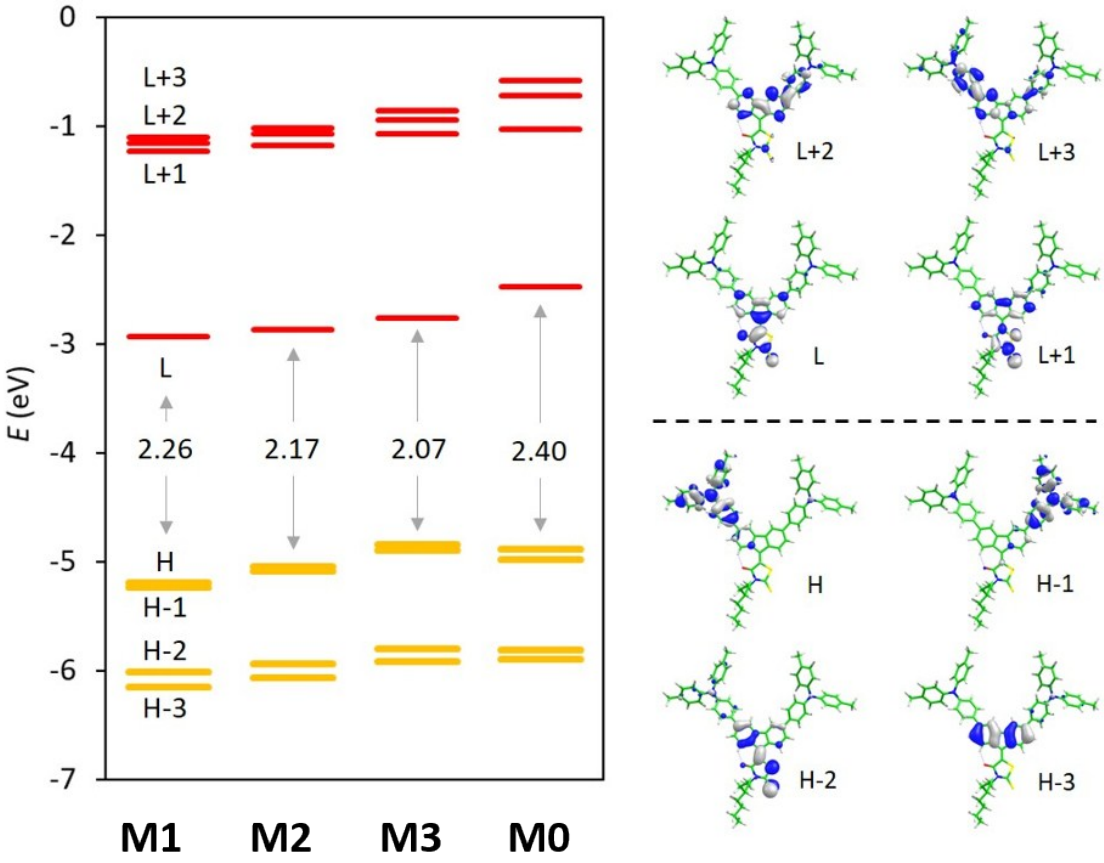

Fig. S3 Left: frontier molecular orbitals diagram calculated for **M0**–**3** at the B3LYP/cc-pVDZ level. Right: frontier molecular orbital topologies (isovalue contours of ±0.03 a.u.) computed for **M2**. H and L denote HOMO and LUMO, respectively.

Particularly different is the case of the rhodanine-based derivative **M0**. In this system, the HOMO and HOMO–1 significantly spread over the fluorene–rhodanine core with an increased π-delocalization due to the direct linkage of the diphenylamine (DPA) donor moiety to the fluorene core through the N atom (Fig. S4). Likewise, the LUMO reaches the donor nitrogen atom of the DPA units with an additional antibonding interaction. As a consequence, the HOMO gains an additional stabilization whereas the LUMO is significantly destabilized in comparison with the analogous **M3** derivative (Fig. S3).

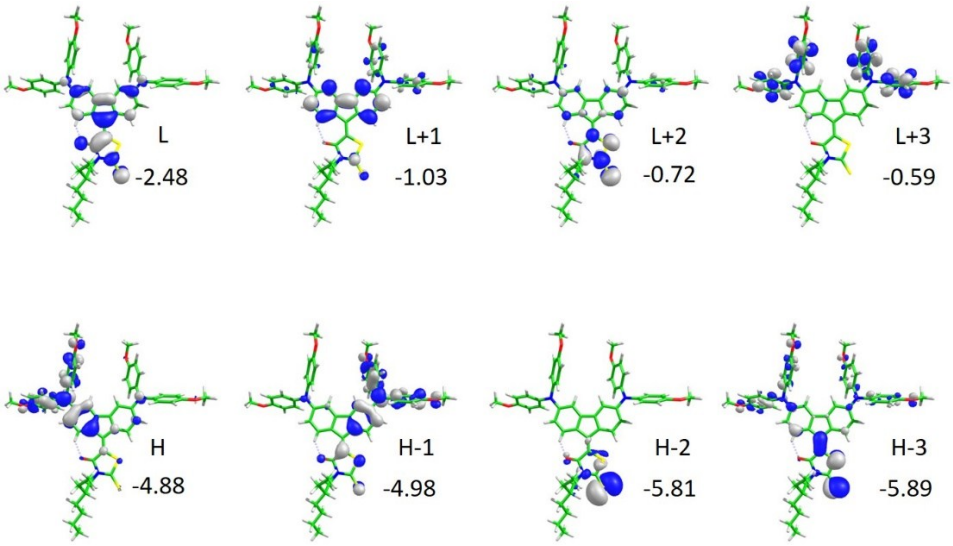

Fig. S4 Frontier molecular orbitals topologies (isovalue contours of ±0.03 a.u.) computed for **M0**. Energy values are indicated in eV. H and L denote HOMO and LUMO, respectively.

4.3. TDDFT Analysis

In order to shed light into the electronic transitions that give rise to the experimental absorption spectra, the 40 lowest-lying singlet excited states were calculated under the time-dependent DFT (TDDFT) framework at the B3LYP/cc-pVDZ level of theory.

Table S2 summarizes the most relevant electronic excitations with a significant intensity in the visible range and their corresponding electronic nature. For **M0**–**3** compounds, TDDFT calculations predict two low-lying singlet excited states, S_1 and S_2, close in energy with a moderate oscillator strength (*f*) between 0.20 and 0.40. These electronic states are described by one-electron promotions from the HOMO and HOMO–1 (localized on the donor TPA units) to the LUMO (centred on the fluorene-rhodanine core), respectively, and thus possess a charge-transfer nature. Interestingly, S_1 and S_2 are predicted to decrease in energy moving from **M1** to **M2** and to **M3** (Table S2), as the electron-donor character of the TPA-substituted moieties increases (from –H to –Me and to –OMe, respectively). For example, S_1 is predicted to decrease in energy from 1.94 eV in **M1** to 1.86 eV in **M2** and to 1.78 eV in **M3**. These results are in good agreement with the red shift experimentally recorded in the absorption spectra going from **M1** to **M3** (Fig. 2a, main text), and with the lowering of the HOMO–LUMO gap upon increasing the electron-donor character of the TPA moiety (from 2.26 eV in **M1** to 2.07 eV in **M3**; see Fig. S3). For **M0**, the lowest-lying charge-transfer states S_1 and S_2 are predicted well-

separated at 1.97 eV (629 nm) and 2.31 eV (537 nm), respectively, being S_2 much more intense (f = 0.696) than S_1 (f = 0.190), which is in good accord with the experimental band recorded at 550 nm with a shoulder around 650 nm (Fig. 2a, main text).

Moving to higher energies, theoretical calculations predict a singlet excited state S_5 for **M1**, **M2** and **M3** positioned around 2.9 eV and described by a local excitation centred on the fluorene–rhodanine core (Table S2). This electronic excitation is calculated at higher energies (3.1 eV) for **M0**, which nicely correlates with the experimental absorption measurements (Fig. 2a, main text). Finally, a large number of electronic states are predicted in the 250–350 nm range. Among them, the most intense transitions are mainly described by local excitations centred on the electron-donor TPA/DPA moieties and extended to the fluorene core (see, for example, state S_7 of **M1** and **M2** in Table S2).

Table S2. Lowest-lying singlet excited states calculated for **M0**–**3** at the TD-B3LYP/cc-pVDZ level.

Compound	State	E (eV) [a]	E (nm) [a]	f [b]	Monoexcitation[c] (%)		Nature[d]
M0	S_1	1.971	629	0.1900	H → L	85	CT
	S_2	2.310	537	0.6958	H–1 → L	86	CT
	S_5	3.125	397	0.3083	H–3 → L	91	Fl-Rh
	S_{22}	4.070	305	0.1550	H–1 → L+6	52	DPA
M1	S_1	1.937	640	0.2114	H → L	84	CT
	S_2	2.069	599	0.3814	H–1 → L	85	CT
	S_5	2.893	429	0.7675	H–2 → L	92	Fl-Rh
	S_7	3.561	348	0.4447	H → L+3	30	TPA-Fl
					H–1 → L+2	25	TPA-Fl
M2	S_1	1.857	668	0.2235	H → L	86	CT
	S_2	1.987	624	0.3724	H–1 → L	87	CT
	S_5	2.881	430	0.8069	H–2 → L	91	Fl-Rh

	S_7	3.503	354	0.4701	H → L+2	30	TPA-Fl
					H → L+3	25	TPA-Fl
M3	S_1	1.779	697	0.2399	H → L	88	CT
	S_2	1.912	649	0.3719	H–1 → L	89	CT
	S_5	2.856	434	0.8116	H–2 → L	88	Fl-Rh
	S_{12}	3.499	354	0.3133	H → L+1	40	CT
	S_{16}	3.625	342	0.3184	H–1 → L+2	68	TPA-Fl

[a] Vertical excitation energies (in eV and nm). [b] Oscillator strengths. [c] Description in terms of monoexcitations; H and L denote HOMO and LUMO, respectively. [d] Nature of the excited state; the labels CT, Rh, Fl and T(D)PA refer to TPA → Rh-Fl charge-transfer, rhodanine, fluorene and tri(di)phenylamine moieties, respectively.

Note that the prediction of the excited state energies for S_1 and S_2 are underestimated (around 0.3–0.5 eV) with respect to the experiment. It is well-known that CT excitations are commonly underestimated by standard hybrid functionals, especially when the CT excitation implies two orbitals with very weak overlap (as is the case of the HOMO and LUMO in **M1**, **M2** and **M3**). This underestimation is attributed to spurious self-interaction and missing derivative discontinuities, two pervasive problems in density functional theory that are intimately related. Conversely, S_1 and S_2 are predicted in very nice agreement for **M0** compared with the experiments in spite of the similar CT nature of the transition. In this case, the absence of a phenyl ring between the nitrogen of DPA and the fluorene core provokes that the HOMO and HOMO–1 spread over the fluorene core and, thus, the overlap between these orbitals and the LUMO is large enough for B3LYP to give an accurate estimation of the CT band position.

4.4. Analysis of φ_S

To deepen into the understanding on why B3LYP predicts accurate CT states in the case of **M0** but significantly underestimates them for TPA-based **M1**, **M2** and **M3**, we calculated the quantum mechanical descriptor φ_S developed by Assfeld et al.,[8] which

consists in a measurement of the spatial overlap between the detachment/attachment densities associated to the electronic transition in the 3D-real space. Note that a low value (close to zero) for the φ_S index implies that the considered excited state has a long-ranged charge-transfer character. Conversely, a φ_S value close to one depicts a local nature for the excited state.

An estimation of φ_S has been performed for the lowest-lying CT states S_1 and S_2 of our rhodanine-based derivatives from a Löwdin charge population scheme using the NANCY_EX (version 2.0) software. Theoretical calculations predict φ_S values for **M1–3** around 0.35–0.37. Otherwise, φ_S values of 0.51 and 0.62 are predicted for S_1 and S_2, respectively, in the case of **M0** (see Fig. S5 for a 3D-representation of the attachment and detachment densities). Noteworthy, a value for the descriptor φ_S = 0.4 is set to differentiate small (φ_S < 0.4) and large (φ_S > 0.4) overlap between detachment and attachment densities.[8] For excitations with small detachment/attachment overlap, standard hybrid functionals start to fail and a range-separated functional is required. These results support the accurate prediction of the CT states in case of **M0** using B3LYP, whereas a large underestimation is calculated for **M1**, **M2** and **M3**.

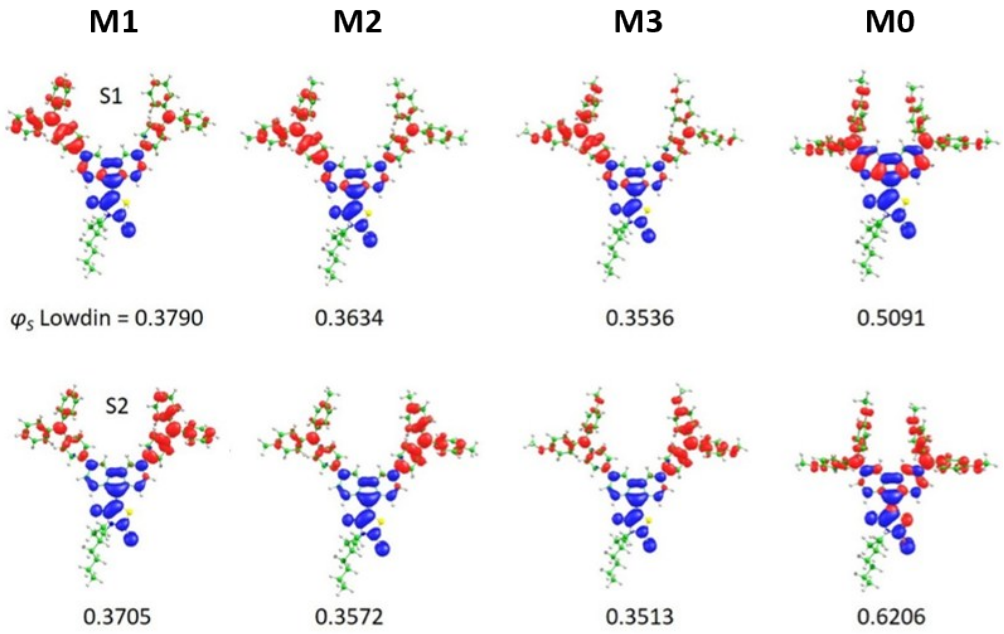

Figure S5. Detachment (red) and attachment (blue) densities calculated for **M0**–**3** with the calculated φ_S descriptor for states S_1 (top) and S_2 (bottom).

In view of the small values of the φ_S descriptor predicted for the S_1 and S_2 states of the TPA-based derivatives, range-separated functionals are therefore required in order to provide an accurate estimation of the lowest-lying CT electronic excitations. Preliminary calculations using the well-known range-separated CAM-B3LYP functional[9] led to unsatisfactory results, with overestimations of the CT band in more than 0.5 eV compared to the experimental data. Moreover, the local excitations were predicted at too higher energies, therefore providing in general worse results than the standard B3LYP functional.

Baer et al. recently reported a simple, physically motivated, first principles *γ*-determining step for the use of range-separated hybrid functionals in quantitative prediction of CT excitation energies.[10] This procedure has been applied lately with much success in the non-empirical tuning of CAM-B3LYP and other long-range corrected functional for prediction of CT excitation energies.[11] Inspired by these works, we decided to incorporate the general expression of the long-range correction (LC) to the pure GGA Becke88 Lee-Yang-Parr BLYP functional and fine-tune the range-separating parameter *γ* to minimize the following function:

$$J(\gamma) = \left|\varepsilon_H(N;\gamma) + IP(N;\gamma)\right| + \left|\varepsilon_H(N+1;\gamma) + IP(N+1;\gamma)\right| \qquad \textbf{(S1)}$$

where ε_H and IP are the HOMO energy and the ionization potential, respectively, of the neutral *N* or anion *N*+1 species as a function of *γ*.

Fig. S6 displays the evolution of $J(\gamma)$ as a function of *γ* going from 0.0 to 1.0 in steps of 0.05 for the **M1** derivative. Theoretical calculations predict the minimum of the $J(\gamma)$ function for a value of *γ* = 0.15. Importantly, the same optimal value was obtained upon analyzing the **M0** system. We therefore use the value of *γ* = 0.15 in the construction of a non-empirically tuned LC-BLYP functional for the subsequent analysis of the CT excitation energies in the series of rhodanine-based derivatives.

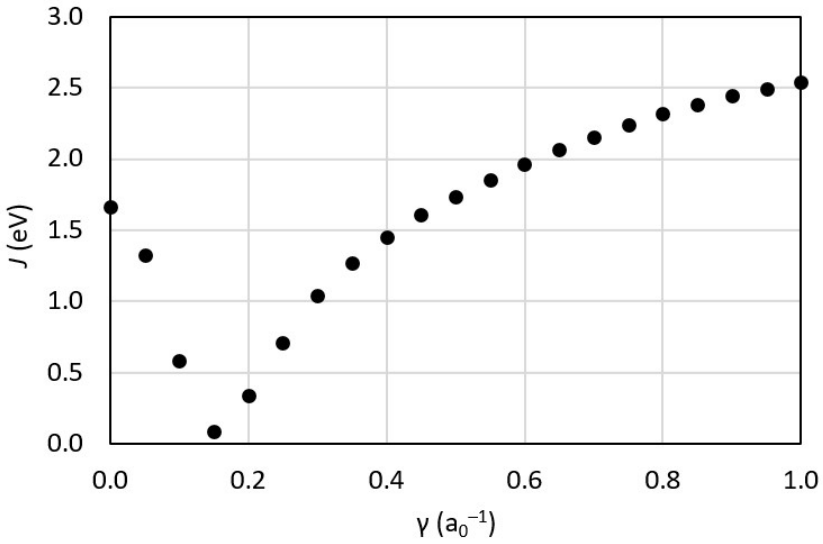

Figure S6. Evolution of *J* as a function of the range-separating parameter *γ* in the **M1** system.

After the optimally-tuned process, TDDFT calculations were therefore carried out for the different compounds using the LC-BLYP functional with the optimal value for the range-separating parameter *γ* = 0.15. Table S3 summarizes the lowest-lying singlet excited states calculated for **M0**–**3** at the LC-BLYP(0.15)/cc-pVDZ level and Fig. 2b (main text) displays the simulation of the theoretical absorption spectra upon convolution of the excitation transitions with Gaussian functions of FWHM = 0.1 eV. The experimental absorption spectra for **M0**–**3** are shown in Fig. 2a. The whole discussion of the simulated absorption spectra and the involved electronic transitions is given in the main text.

Table S3. Lowest-lying singlet excited states calculated for **M0**–**3** at the TD-LC-BLYP(0.15)/cc-pVDZ level.

Compound	State	*E* (eV) [a]	*E* (nm) [a]	*f* [b]	Nature
M0	S_1	2.155	575	0.1775	CT
	S_2	2.491	498	0.9115	CT
	S_6	3.425	362	0.2559	DPA → Fl
	S_{17}	4.088	303	0.2133	TPA
M1	S_1	2.411	514	0.1633	CT
	S_3	2.638	470	0.9835	CT

	S_4	2.930	423	0.3215	Fl-Rh
	S_{11}	3.798	326	0.5365	TPA
M2	S_1	2.374	522	0.1897	CT
	S_2	2.584	480	0.6175	CT
	S_3	2.613	475	0.4233	CT
	S_4	2.879	431	0.2968	Fl-Rh
	S_{11}	3.746	331	0.6156	TPA
M3	S_1	2.320	534	0.2232	CT
	S_2	2.543	488	0.9800	CT
	S_4	2.832	438	0.2645	Fl-Rh
	S_{11}	3.718	333	0.8032	TPA

5. Marcus Charge Transfer and Recombination Rates

In order to relate the experimentally obtained rates for geminate recombination to the electronic and geometrical structure of the donor molecules, we use the Marcus-Jortner equation, explicitly taking into account electron-phonon coupling (inner reorganization).[12]

$$k_{CR} = \sqrt{\frac{\pi}{\hbar^2 \lambda_{ext}(r) k_B T}} |V(r,p)|^2 \sum_{\nu=0}^{\infty} \frac{e^{-S} S^{\upsilon}}{\upsilon!} exp[\frac{-(\nu E_{\upsilon} + \lambda_{ext}(r) + \Delta G_{CR}^{0}(r))^2}{4\lambda_{ext}(r) k_B T}] \quad \text{(S3)}$$

where the Huang-Rhys factor is given by $S = \lambda_{int}/E_{\upsilon}$, λ_{int} being the internal reorganization energy and E_{υ} the vibrational energy of an effective mode (we assume 0.2 eV, equivalent with the dominant C=C stretch vibration). The external reorganization energy is given by $\lambda_{ext}(r)$, where r is the center-to center distance of the oxidized donor (**D**) and reduced acceptor (**A**) excess charge densities (see ESI), υ is the vibrational quantum number, V is the coupling between **D** and **A**, k_B is Boltzmann's constant, and $\Delta G_{CR}^{0}(r)$ is the Gibbs free energy change ("driving force") for charge recombination.

Ignoring entropy contributions to the driving force, we can express ΔG_{CR}^{0} as the difference of the minima of the potential energy surfaces of the final and initial states for charge recombination, $E_f(\chi)$ and $E_i(\chi)$, respectively, both depending on the polarization coordinate χ:

$$\Delta G_{CR}^{0} = min(E_f^Y(\chi)) - min(E_i^Y(\chi)) \quad \text{(S4)}$$

$$\Delta G_0^{CR} = -\left(E_{ox}^{D} - E_{red}^{A} + k\left(\frac{-1}{2\varepsilon_{ref} r_d} - \frac{1}{2\varepsilon_{ref} r_a} + \frac{1}{2\varepsilon_r r_d} + \frac{1}{2\varepsilon_r r_d}\right) + E_c\right), \quad k = q^2/(4\pi\varepsilon_0) \quad \text{(S5)}$$

where E_{ox}^{D} and E_{red}^{A} are the oxidation potential of the donor and the reduction potential of the acceptor, respectively, as measured by cyclovoltammetry, performed in a solvent in which the relative dielectric constant is ε_{ref} (for dichloromethane, ε_{ref} = 8.93). The correction terms in the bracket account for the fact that in the donor-acceptor blend, the effective relative dielectric constant ε_r is different from that of the solvent in which the oxidation and reduction potentials have been obtained (Rehm-Weller equation). In agreement with other authors [Caruso, PNAS], here we assume ε_r = 3.6. The single terms in the bracket are solvation energies, for which we use the Born equation, assuming a spherical cavity of radius r_a and r_d for acceptor and donor, respectively. For the calculation of r_a and r_d, we assumed a sphere of the same volume that the respective molecule would consume at a specific density of ρ=1.2 g/cm^3.

The Coulomb energy is given by:

$$E_C = \sum \frac{q_d q_a}{4\pi\varepsilon_0\varepsilon_r r} \quad \text{(S6)}$$

Sample	λ_{int}	λ_{ext}	ΔG_{CR}^{0}
M0:PCBM 1:3	0.154	0.12	1.66
M1:PCBM 1:3	0.112	0.118	1.86
M2:PCBM 1:3	0.106	0.114	1.71
M3:PCBM 1:3	0.14	0.11	1.59

Table S4. internal and external reorganization energies λ_{int} and λ_{ext}, respectively, given in eV. Internal reorganization energies calculated by geometry optimization of the respective molecules in their neutral and charged states, external reorganization energies calculated by

$$\lambda_{ext} = k * (1/\varepsilon_{inf} - 1/\varepsilon_r) * (1/(2 * r_a) + 1/(2 * r_d) - 1/r_{DA}) \quad \text{(S7)}$$

Where we assume ε_{inf} = 2.4

Finally, the driving force ΔG_{CR}^{0} was obtained using eq. S5.

6. Global and Target Analysis

Femtosecond transient absorption (TA) spectroscopy is used to trace photophysics that occur on a time scale of femto to picoseconds. However, the spectral signatures of photoexcited states in TA spectra generally overlap, so matrix decomposition techniques need to be used to obtain the time-resolved populations of the various photoexcited states separately. The mathematics of the procedure has been described by van Stokkum *et al.*[13] Here, we generalize to arbitrary photoexcitation dynamics.

We apply Beer-Lambert's Law,

$$A_c(t,\omega) = \sum_i c_i(t)\sigma_i(\omega) \quad \text{(S7)}$$

to find the calculated transient absorption $A_c(t,\omega)$ reproducing the measured transient absorption spectrum $A(t,\omega)$, which depends on time t and probe energy ω, by a superposition of states i with characteristic time-resolved concentration $c_i(t)$ and energy-dependent absorption cross-section $\sigma_i(\omega)$. Eq. S7 can be written in matrix form:

$$A_c = c \times \sigma \quad \text{(S8)}$$

In eq. S8, each column of the c matrix represents one complete concentration-time dependence of a state i, while each row of the σ matrix represents the full (time-invariant) spectrum of that state i. Of course, any linear combination σ' of the spectra in the σ matrix

$$\sigma' = s \times \sigma \tag{S9}$$

s being the spectral weight matrix, can also solve eq. S8, as can be seen by introducing S9 into S8:

$$A_c = c \times s^{-1} \times \sigma' \tag{S10}$$

and substituting $c \times s^{-1} \equiv c'$:

$$A_c = c' \times \sigma' \tag{S11}$$

Comparing eqs. S11 and S8 highlights the crux in global spectral modeling: There is an infinite number of combinations of *c'* and *σ'* that all reproduce the measured TA spectra perfectly. Our goal is to find the photophysical dynamics *c* and the photophysical spectra *σ*, not some linear combinations *c'* and *σ'*. Multiplying eq. S8 by the inverse matrix of the spectra, σ^{-1}, we get

$$A_c \sigma^{-1} = c \tag{S12}$$

The interpretation of eq. S12 is as follows: as there is only one inverse of the spectra, there is one and only one matrix *c* solving S12. Consequently, if the spectra of the photoexcited states are known, we are guaranteed to find the photophysical concentrations. Vice versa, if the concentrations are known, we are guaranteed to find the photophysical cross-sections.

The time-resolved concentrations c(t) in eq. S12, obtained from spectral modeling of transient absorption matrices A_c measured at different pump pulse energies and thus starting concentrations, are reproduced by numerically solving a rate equation model according to:

$$\frac{dc}{dt} = -k_{ng}^{0} \cdot t^{-\gamma} \cdot c^2 - k_g^0 \cdot t^{-\gamma} \cdot c \tag{S13}$$

Herein, k_{ng}^{0} and k_g^0 are the rate constants for non-geminate and geminate recombination, respectively, of charged states, γ is the dispersiveness parameter (γ = 0 is equivalent to a time-independent rate coefficient) which is due to disorder. The units

are such that $\left[k_{ng}^{0} \cdot t^{-\gamma}\right] = cm^3/s$ and $\left[k_{g}^{0} \cdot t^{-\gamma}\right] = s^{-1}$. We globally fitted numerical solutions of S13, using γ=0.5, to concentration dynamics with different starting concentrations. The results are shown in Figs SXX – Sxx for all synthesized compounds in their 1:3 blends with PCBM.

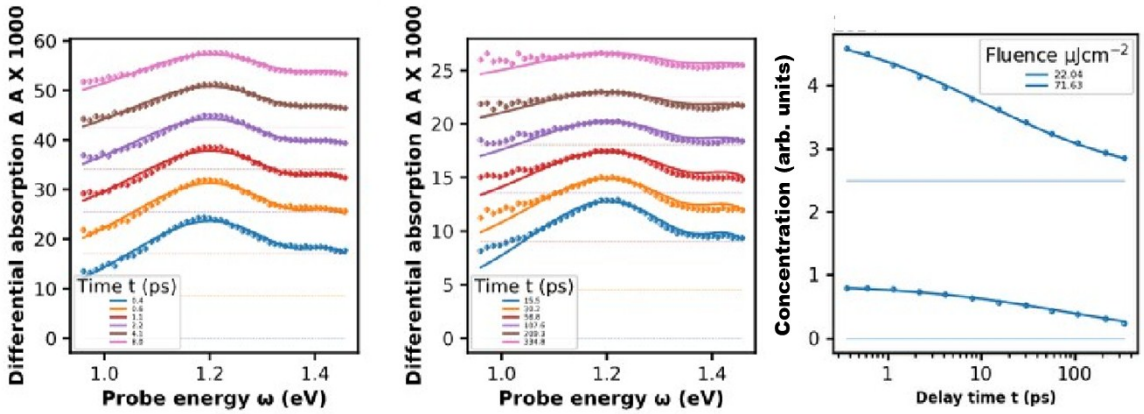

Figure S7: M0:PCBM. Left: TA spectra (symbols) in near infrared spectral region (early times), middle TA spectra (late times). Lines are spectral fits according to eq. S12, yielding time-resolved charge concentrations (symbols in right panel for two different pump intensities, as given in the legend). Lines in the right panel are global fits according to S13, yielding the rate constants given in Table S5. The curves are shifted for clarity of presentation, with baseline indicated as thin horizontal line.

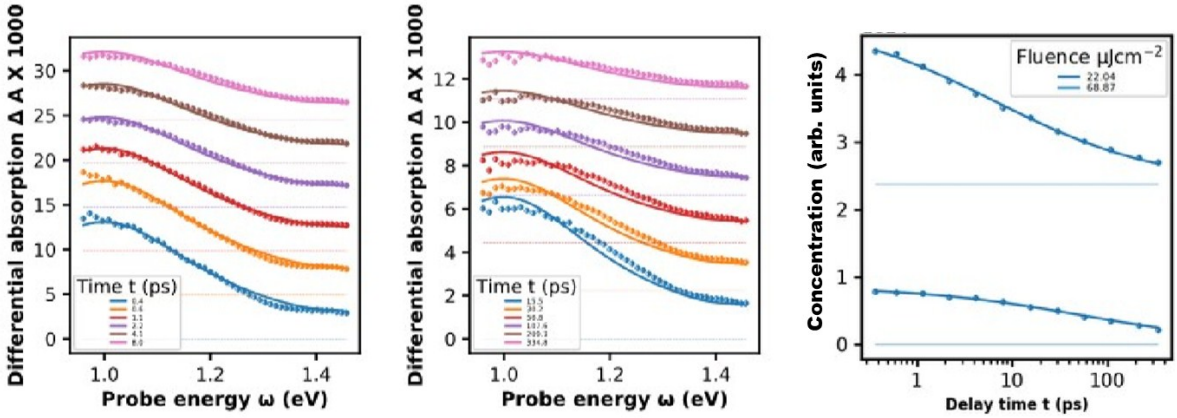

Figure S8. M1:PCBM. Left: TA spectra (symbols) in near infrared spectral region (early times), middle TA spectra (late times). Lines are spectral fits according to eq. S12, yielding time-resolved charge concentrations (symbols in right panel for two different pump intensities, as given in the legend). Lines in the right panel are global fits according

to S13, yielding the rate constants given in Table S5. The curves are shifted for clarity of presentation, with baseline indicated as thin horizontal line.

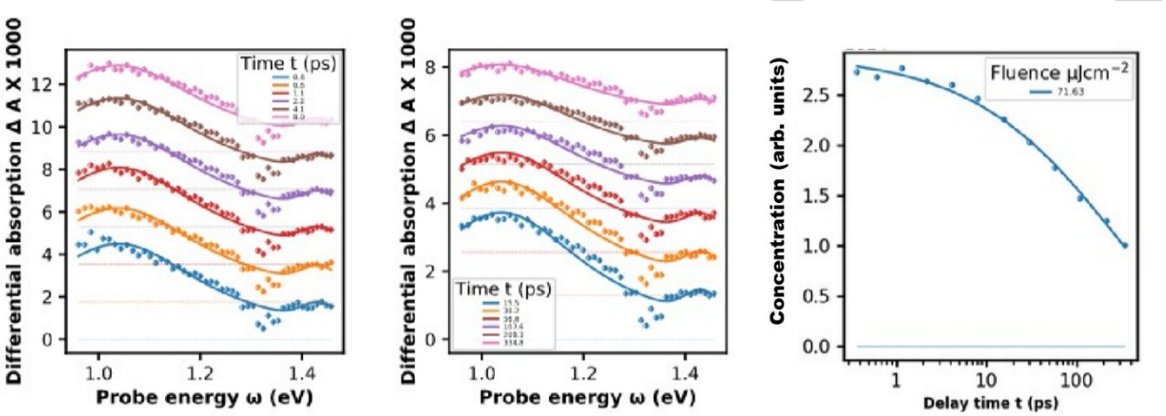

Figure S9. M2:PCBM. Left: TA spectra (symbols) in near infrared spectral region (early times), middle TA spectra (late times). Lines are spectral fits according to eq. S12, yielding time-resolved charge concentrations (symbols in right panel with pump intensity as given in the legend). Lines in the right panel are global fits according to S13, yielding the rate constants given in Table S5. The curves are shifted for clarity of presentation, with baseline indicated as thin horizontal line.

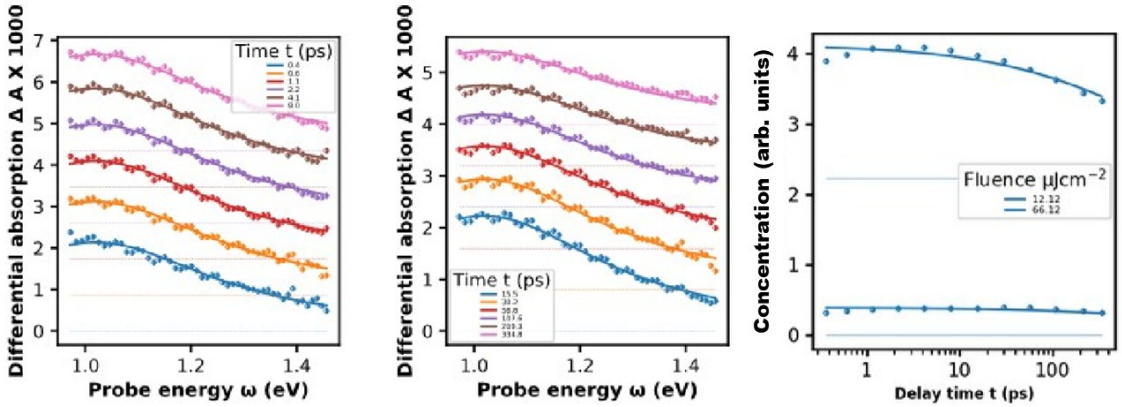

Figure S10. M3:PCBM. Left: TA spectra (symbols) in near infrared spectral region (early times), middle TA spectra (late times). Lines are spectral fits according to eq. S12, yielding time-resolved charge concentrations (symbols in right panel for two different pump intensities, as given in the legend). Lines in the right panel are global fits according to S13, yielding the rate constants given in Table S5. The curves are shifted for clarity of presentation, with baseline indicated as thin horizontal line.

Sample	k_{ng} ($cm^3/s^{1/2}$)	k_g ($s^{-1/2}$)	$\tau_{1/2}$ (ns)
M0:PCBM	6e-15	4e3	7.5
M1:PCBM	8e-15	0	>10
M2:PCBM	3e-16	*	*
M3:PCBM	6e-16	4.4e3	6.2

Table S5. Fitted constants from the global numerical modeling according to S13. Half-life times $\tau_{1/2}$ were obtained by an analytical solution of eq. S13 for k_{ng}=0 and finding $\tau_{1/2}$ by setting $c(\tau_{1/2}) = ½\ c(0)$.

7. NMR & MS Spectra

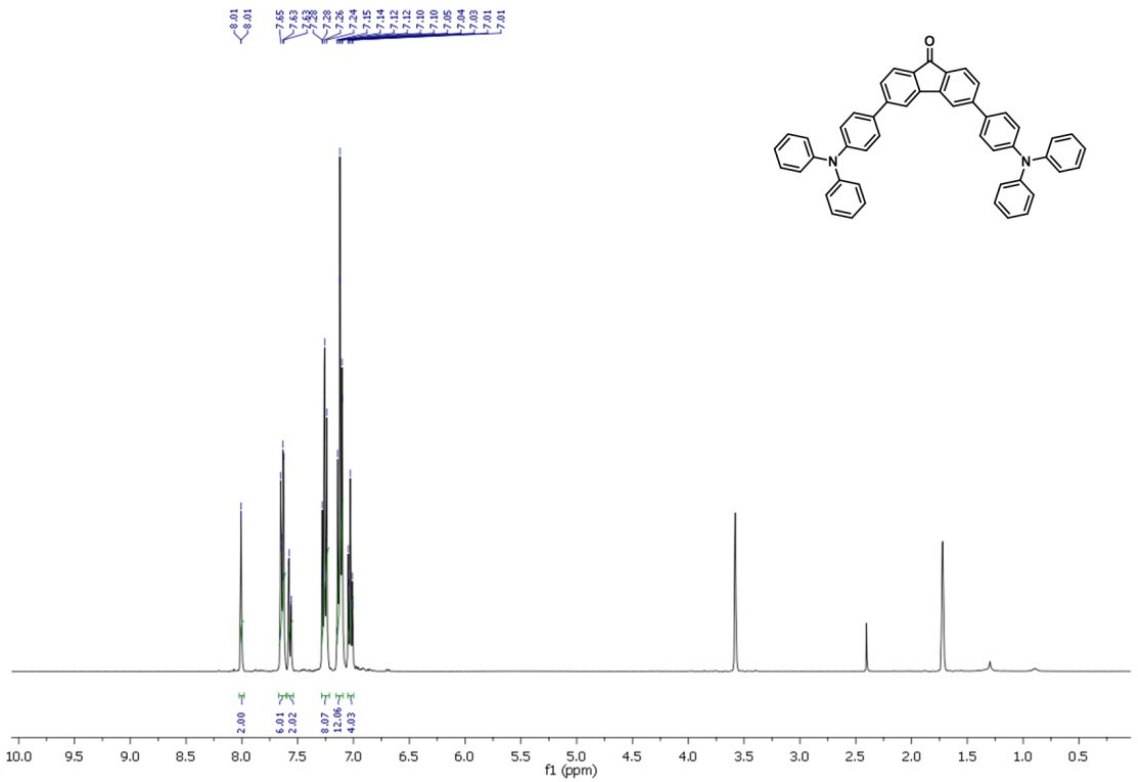

Figure S11. ^{1}H NMR spectrum (400 MHz, THF-d^{8}) of **6**.

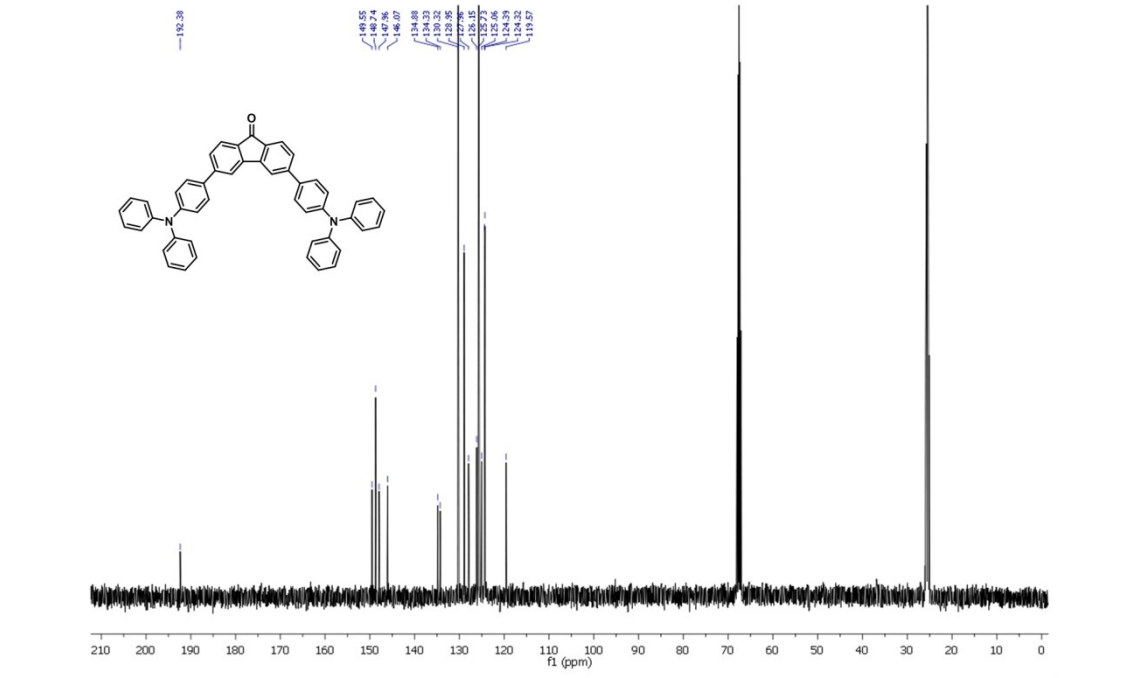

Figure S12. ^{13}C NMR spectrum (101 MHz, THF-d^{8}) of **6**.

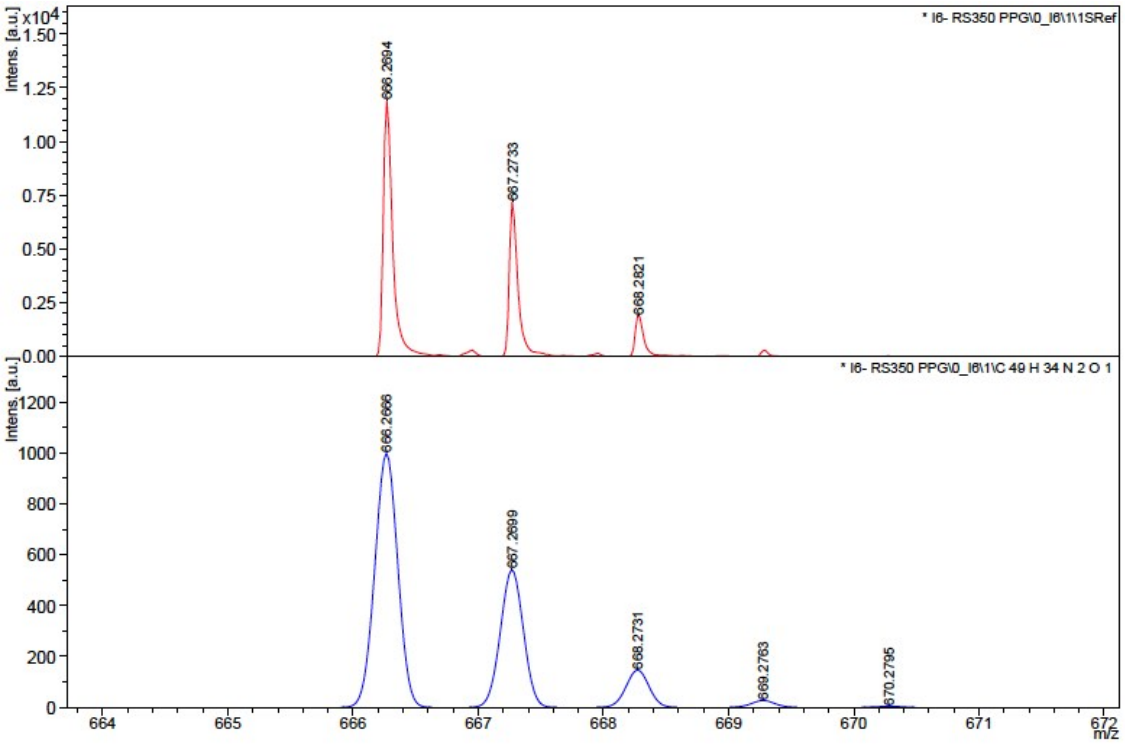

Figure S13. Recorded (top) and simulated (bottom) MALDI-TOF spectra of **6**.

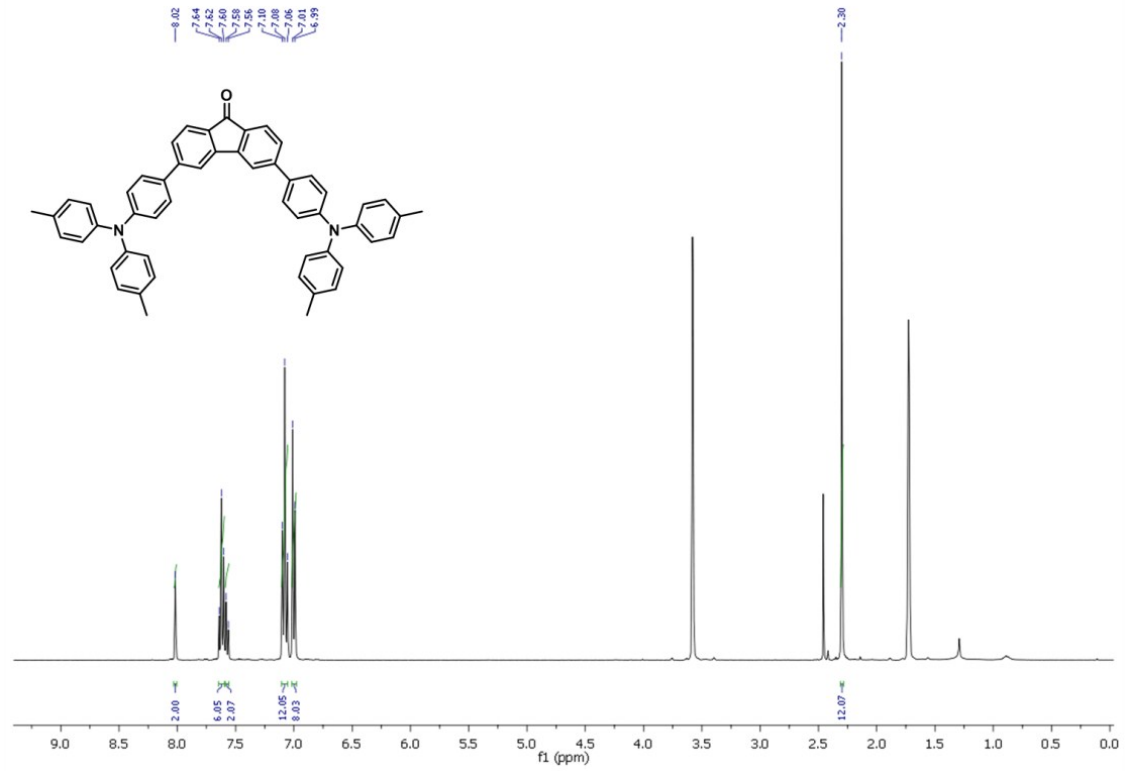

Figure S14. ^{1}H NMR spectrum (400 MHz, THF-d^{8}) of **7**.

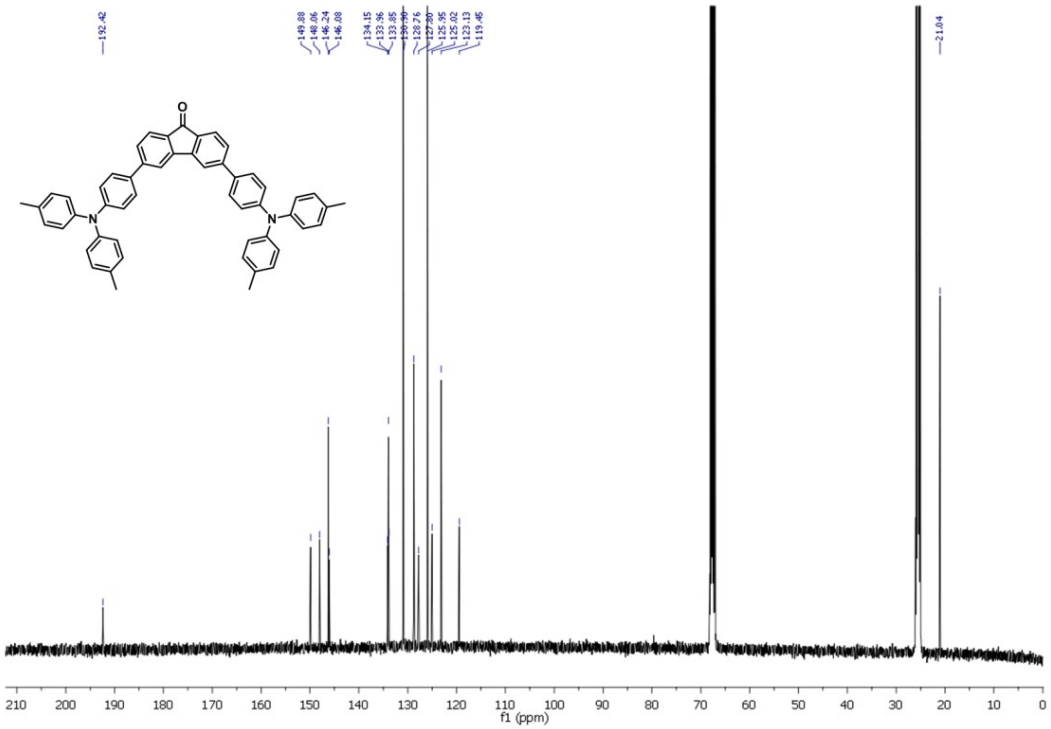

Figure S15. ^{13}C NMR spectrum (101 MHz, THF-d^8) of **7**.

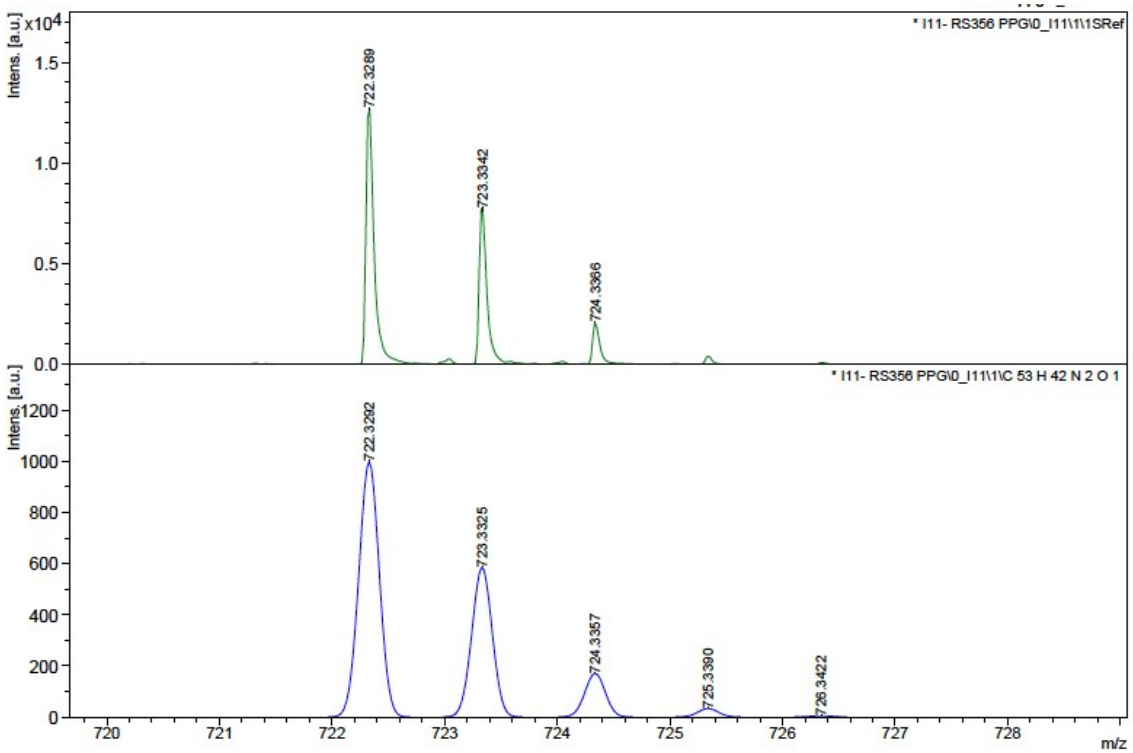

Figure S16. Recorded (top) and simulated (bottom) MALDI-TOF spectra of **7**.

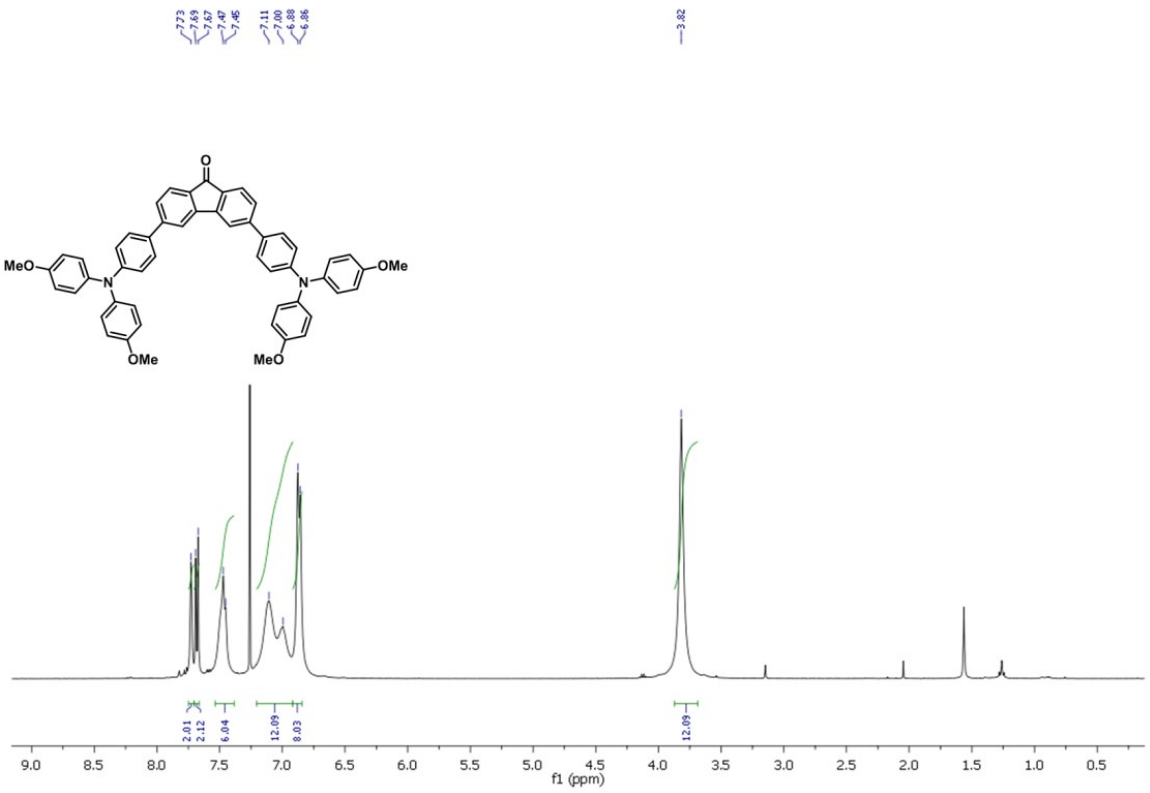

Figure S17. ^{1}H NMR spectrum (400 MHz, $CDCl_3$) of **8**.

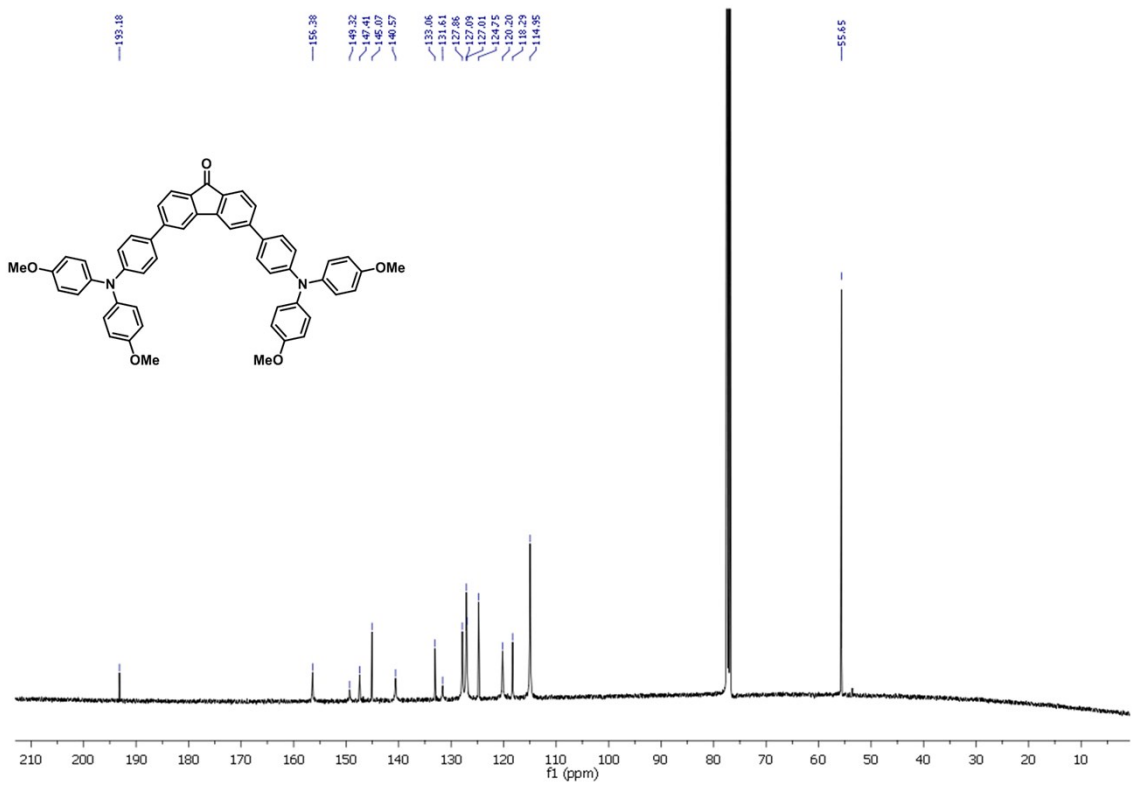

Figure S18. ^{13}C NMR spectrum (101 MHz, $CDCl_3$) of **8**.

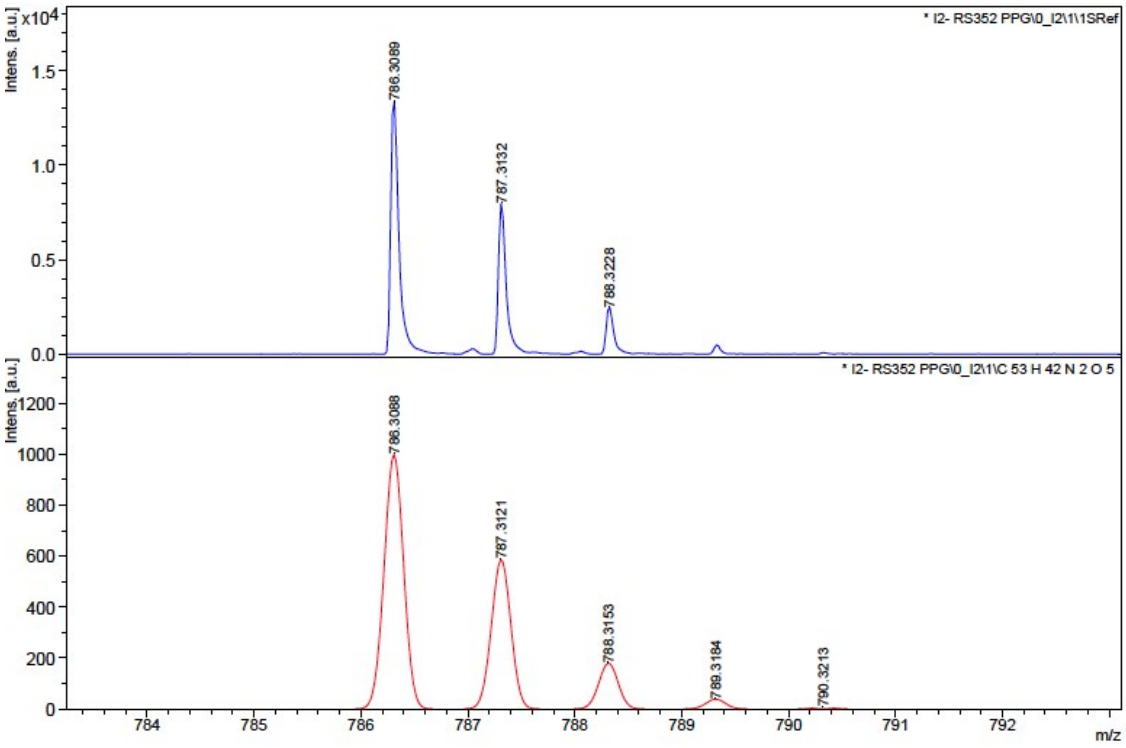

Figure S19. Recorded (top) and simulated (bottom) MALDI-TOF spectra of **8**.

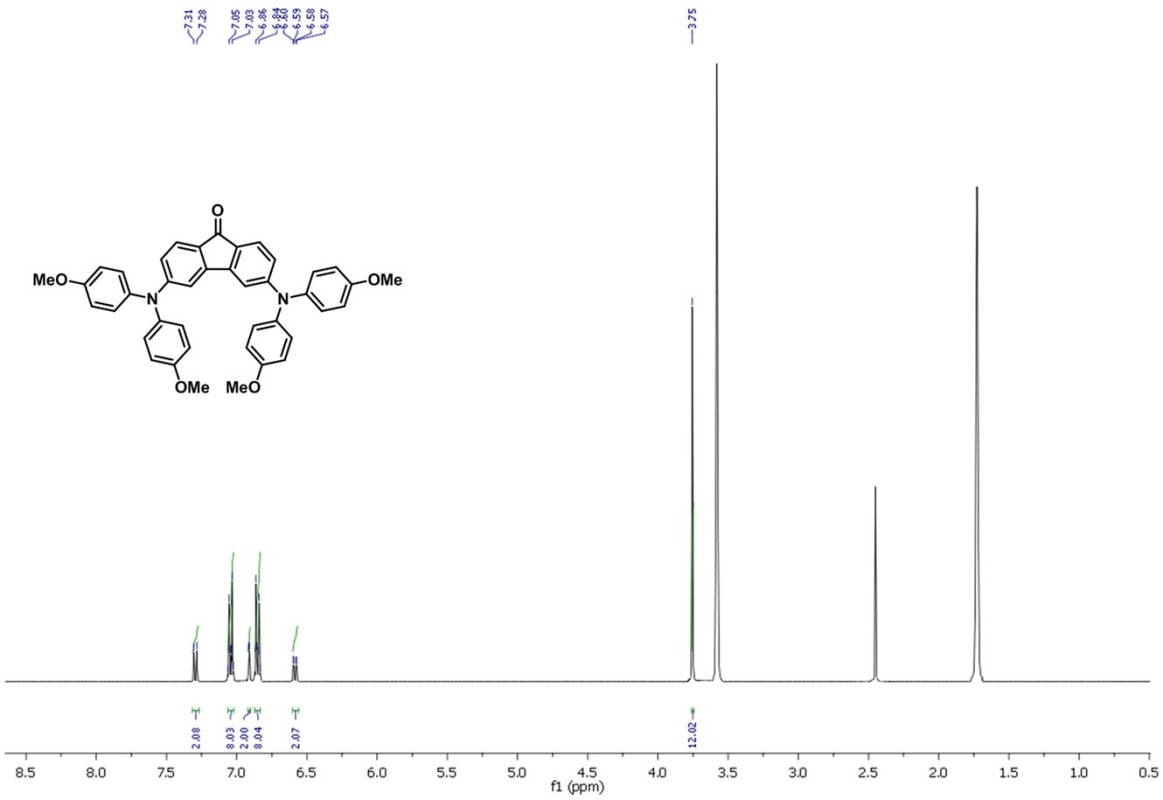

Figure S20. ^{1}H NMR spectrum (400 MHz, THF-d^{8}) of **9**.

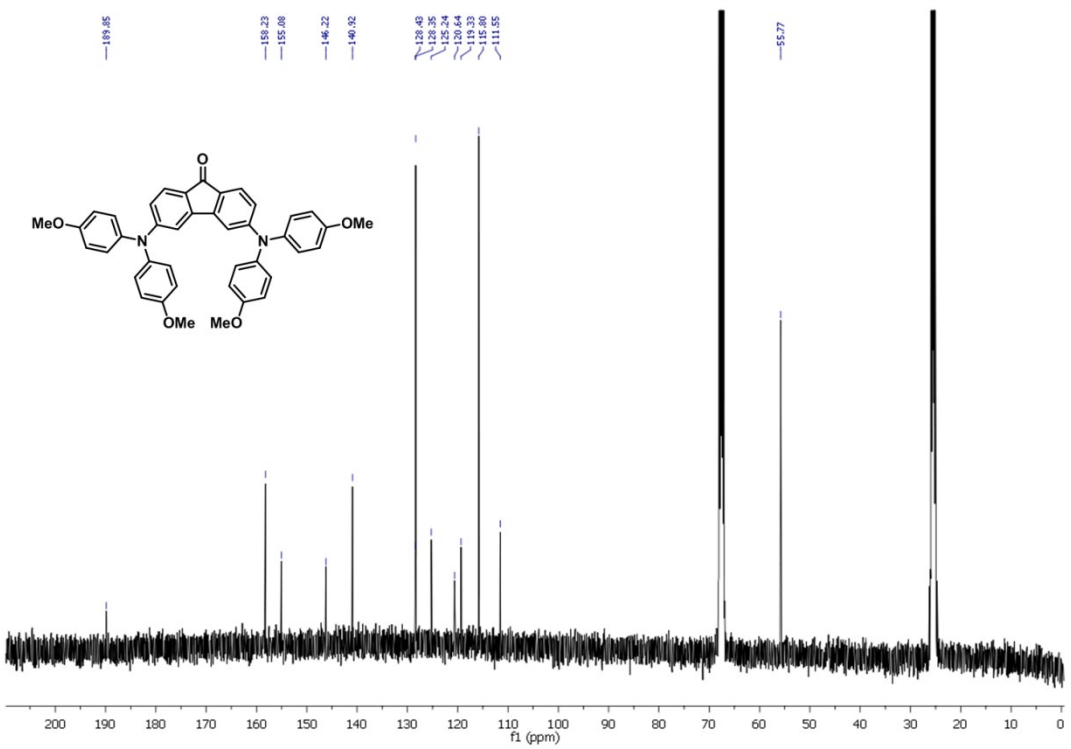

Figure S21. ^{13}C NMR spectrum (101 MHz, THF-d^8) of **9**.

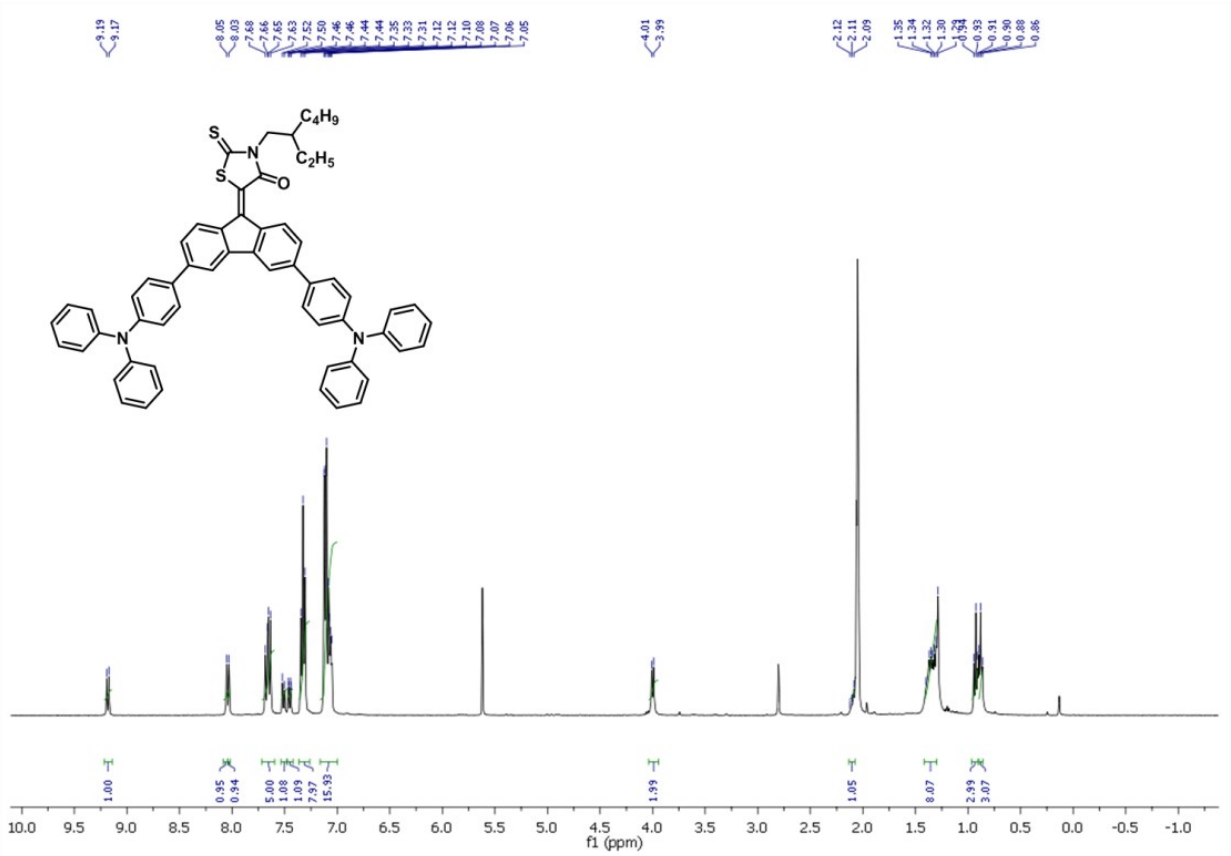

Figure S22. ^{1}H NMR spectrum (400 MHz, Acetone-d^6) of **M1**.

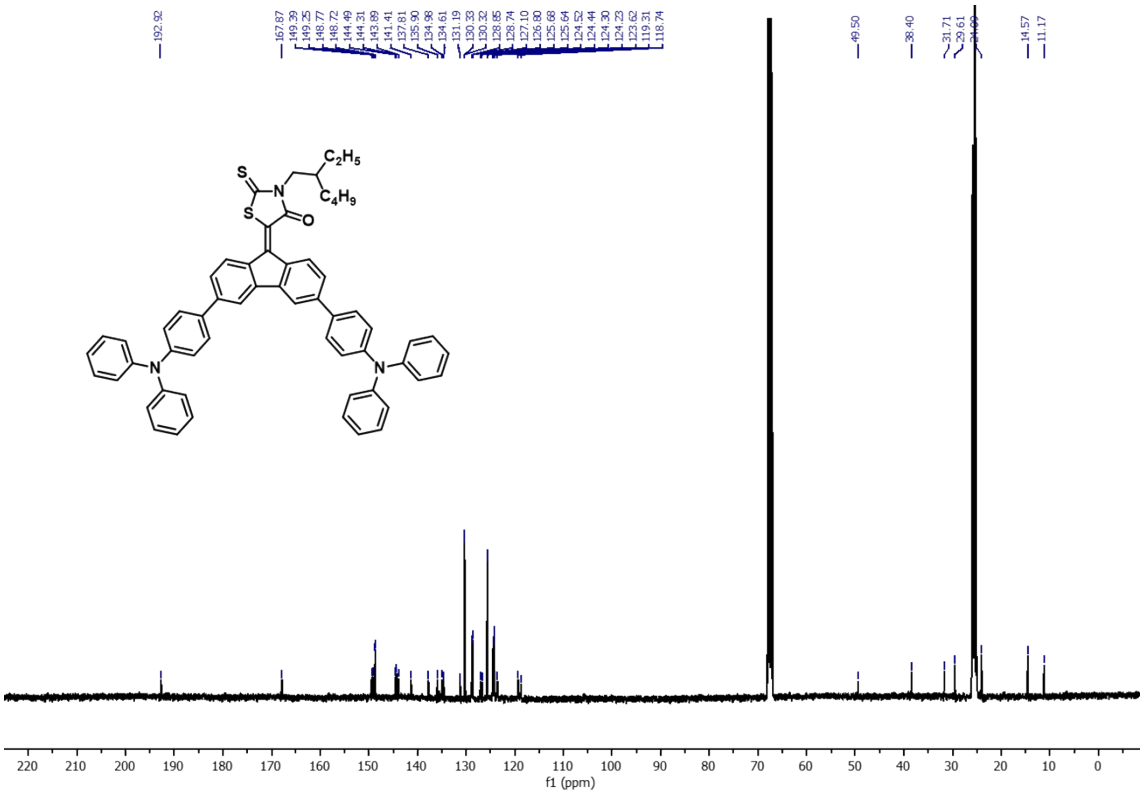

Figure S23. ^{13}C NMR spectrum (101 MHz, Acetone-d^6) of **M1**.

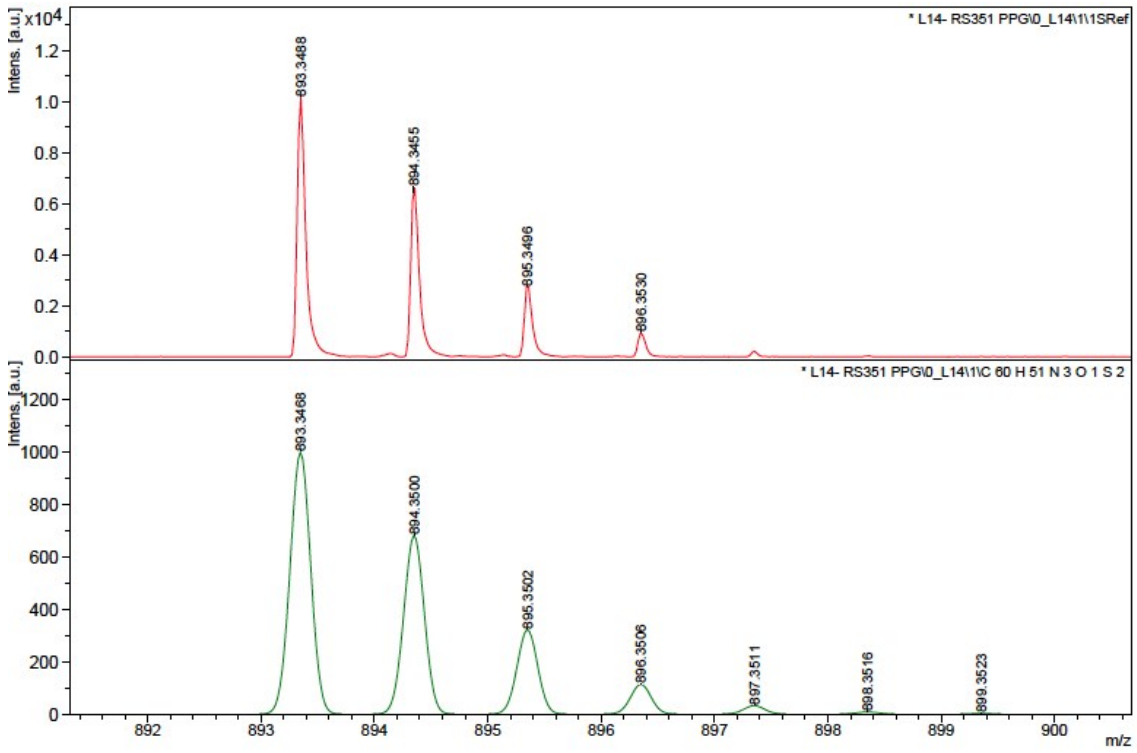

Figure S24. Recorded (top) and simulated (bottom) MALDI-TOF spectra of **M1**.

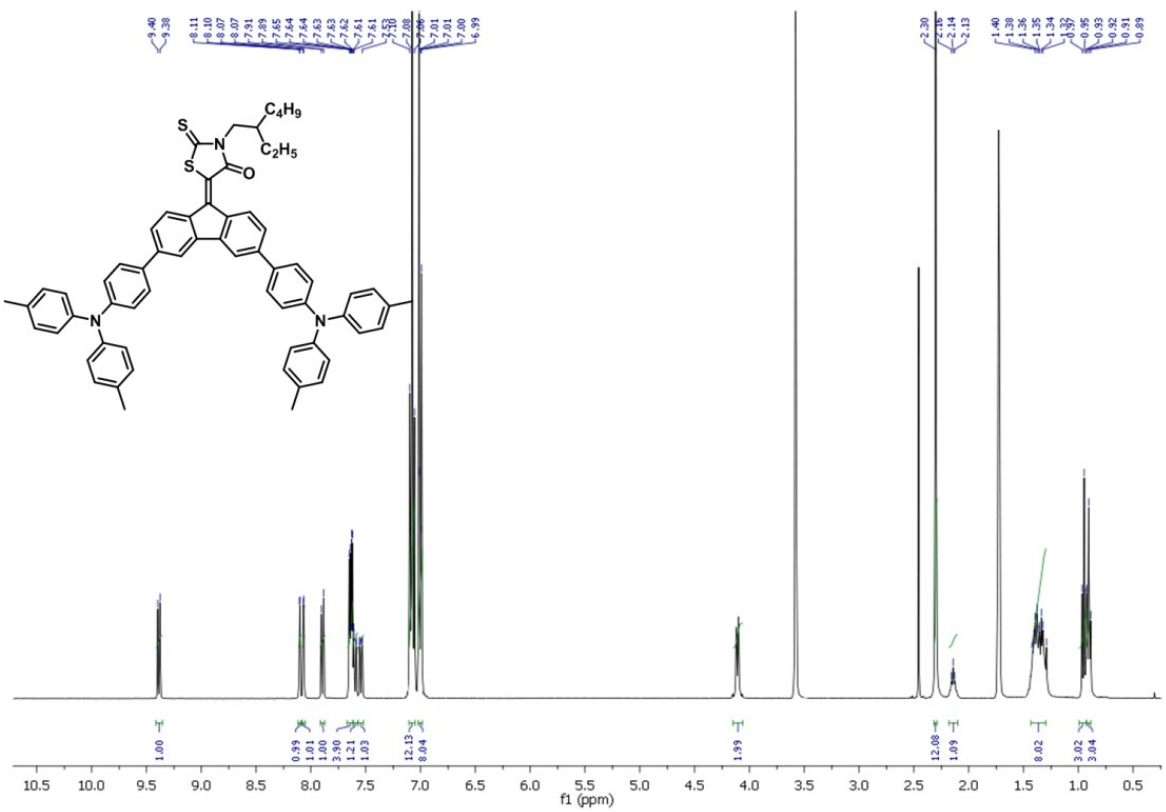

Figure S25. ^{1}H NMR spectrum (400 MHz, THF-d^{8}) of **M2**.

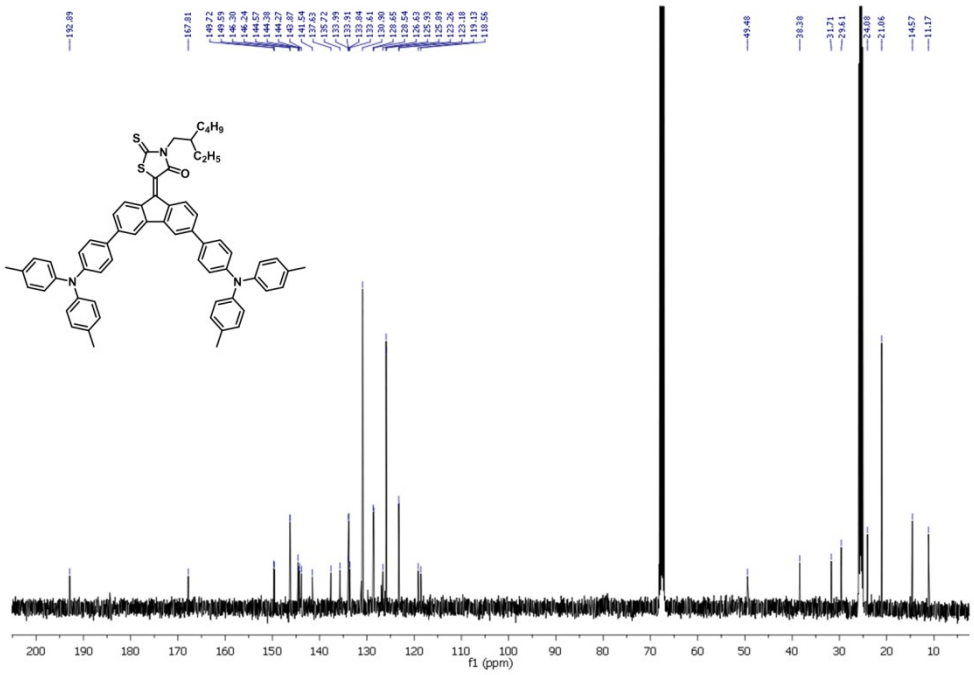

Figure S26. ^{13}C NMR spectrum (101 MHz, THF-d^{8}) of **M2**.

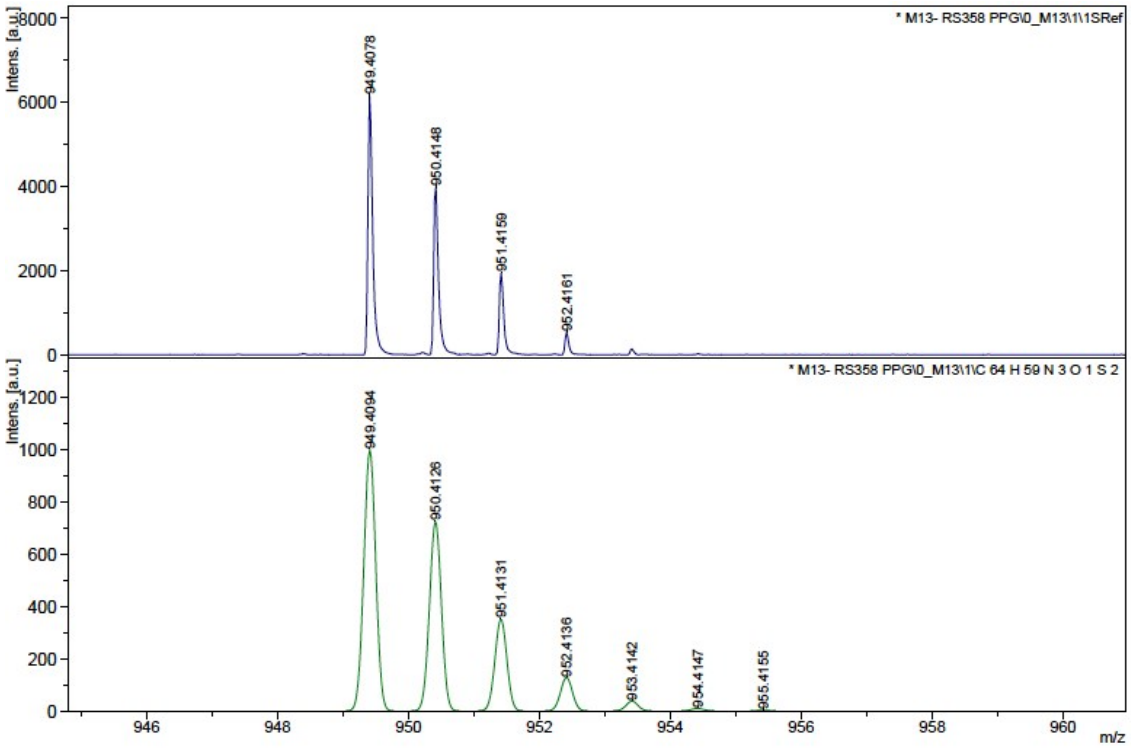

Figure S27 Recorded (top) and simulated (bottom) MALDI-TOF spectra of **M2**.

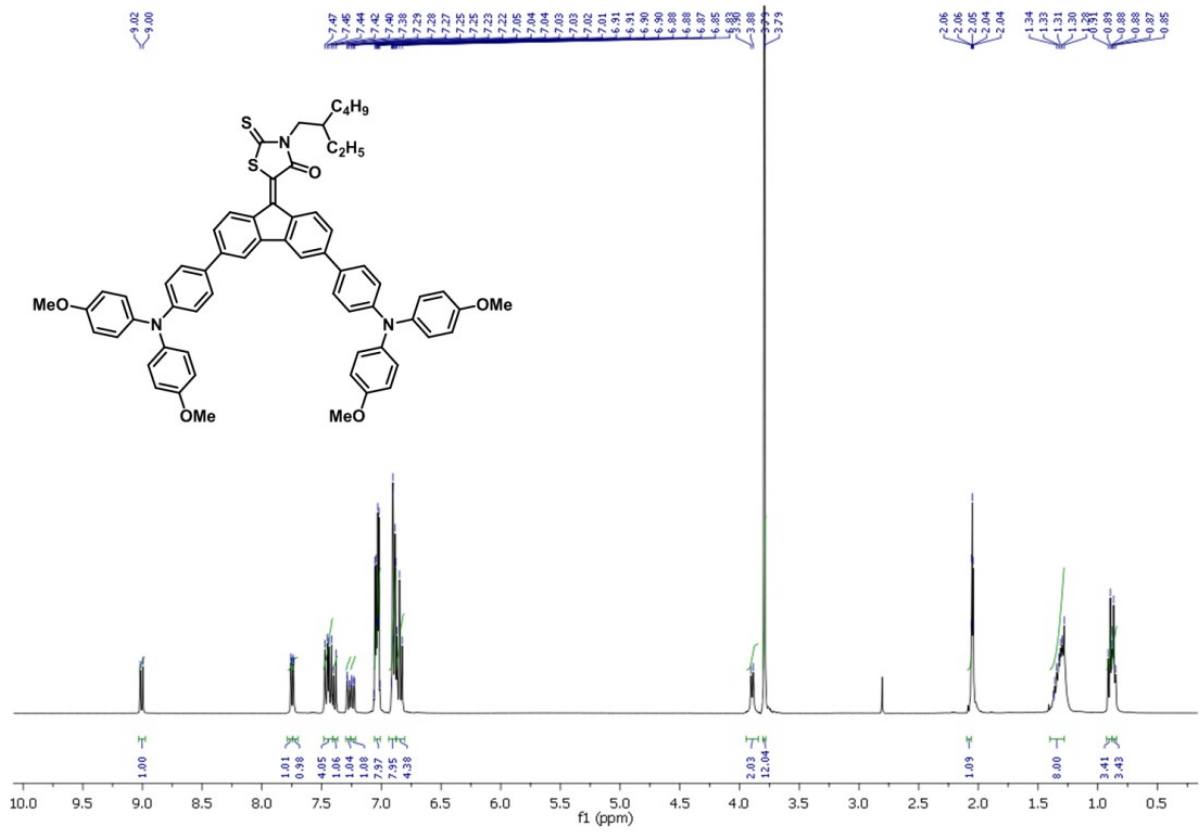

Figure S28. ^{1}H NMR spectrum (400 MHz, acetone-d^{6}) of **M3**.

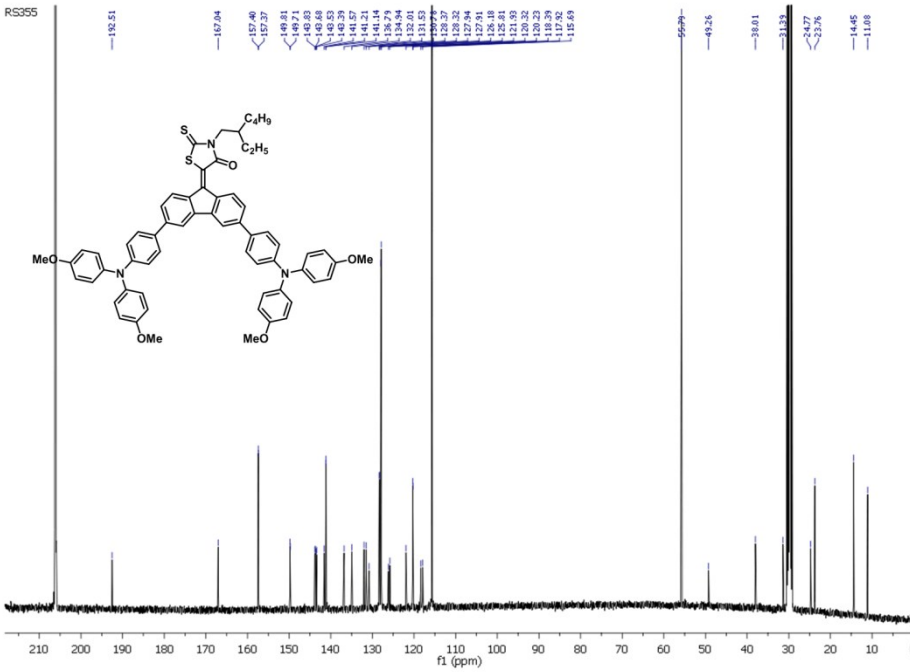

Figure S29. ^{13}C NMR spectrum (101 MHz, acetone-d^6) of **M3**.

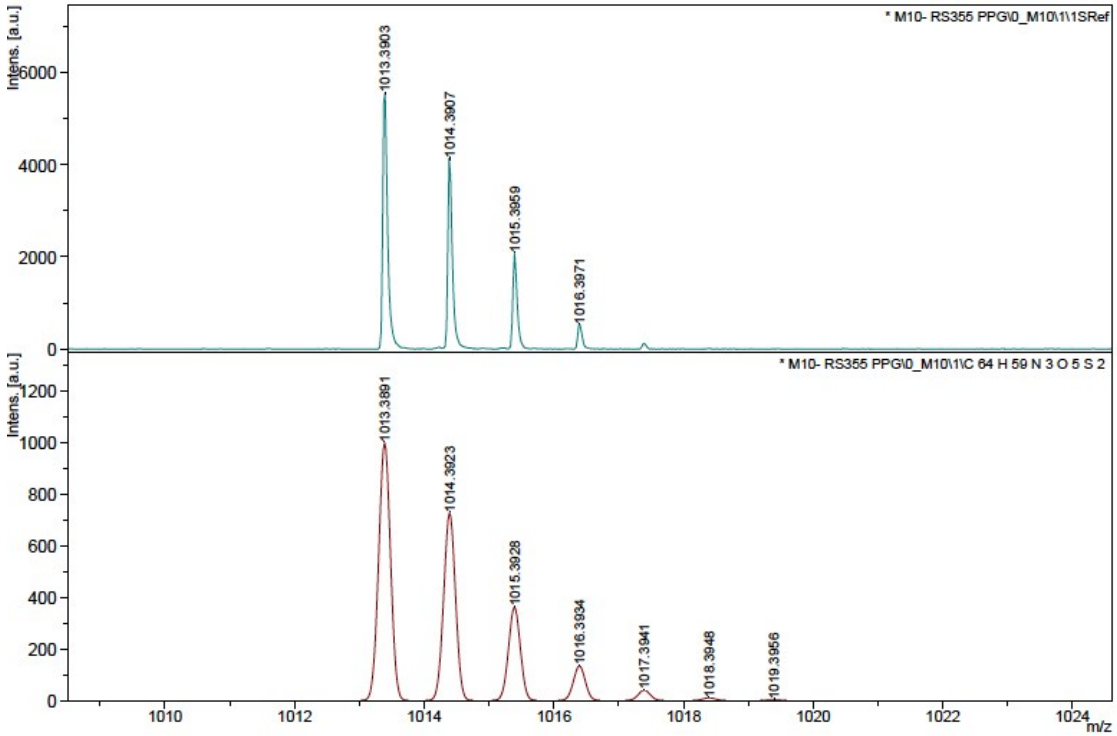

Figure S30. Recorded (top) and simulated (bottom) MALDI-TOF spectra of **M3**.

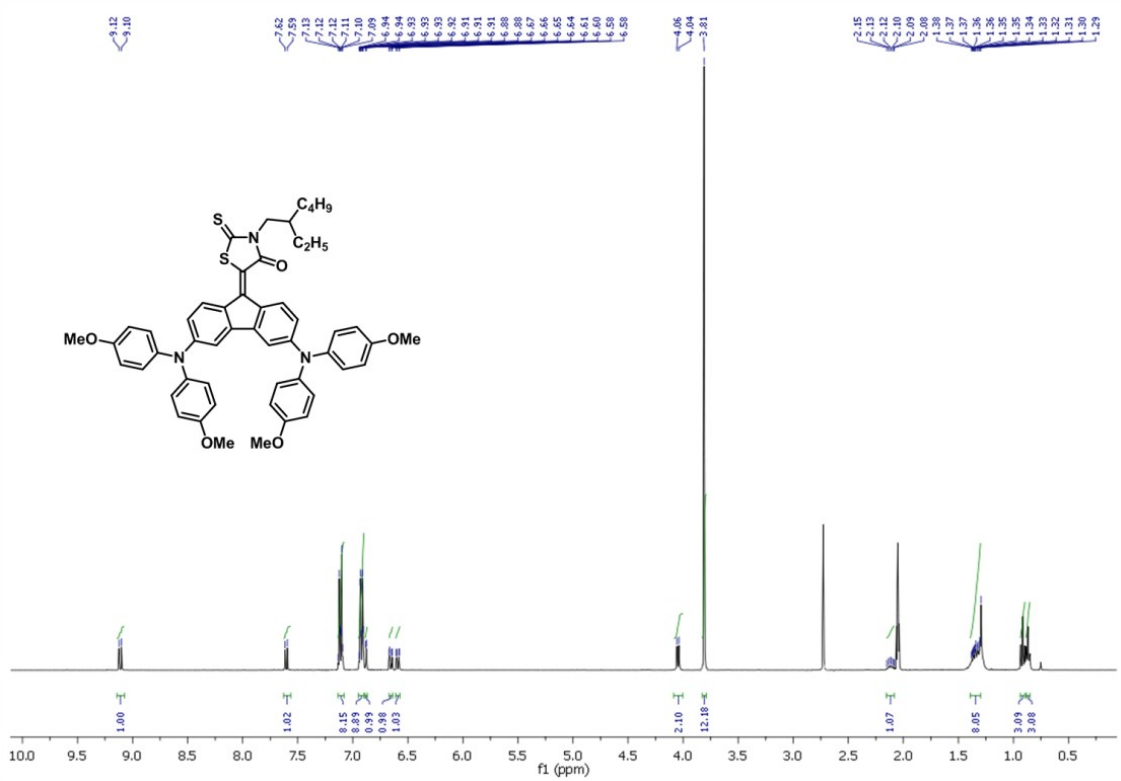

Figure S31. ^{1}H NMR spectrum (400 MHz, acetone-d^{6}) of **M0**.

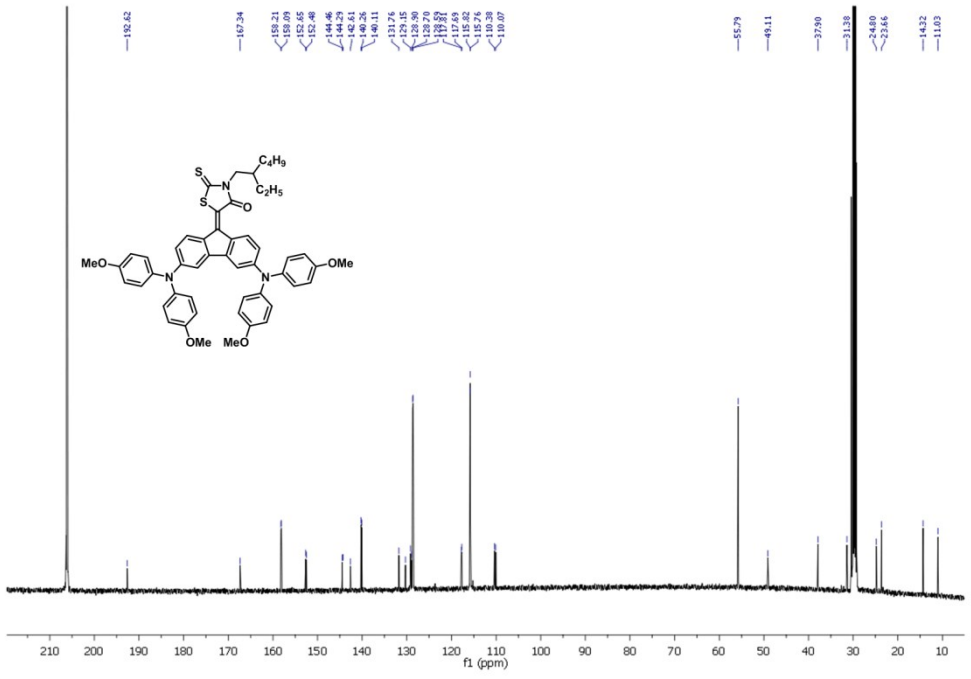

Figure S32. ^{13}C NMR spectrum (101 MHz, acetone-d^{6}) of **M0**.

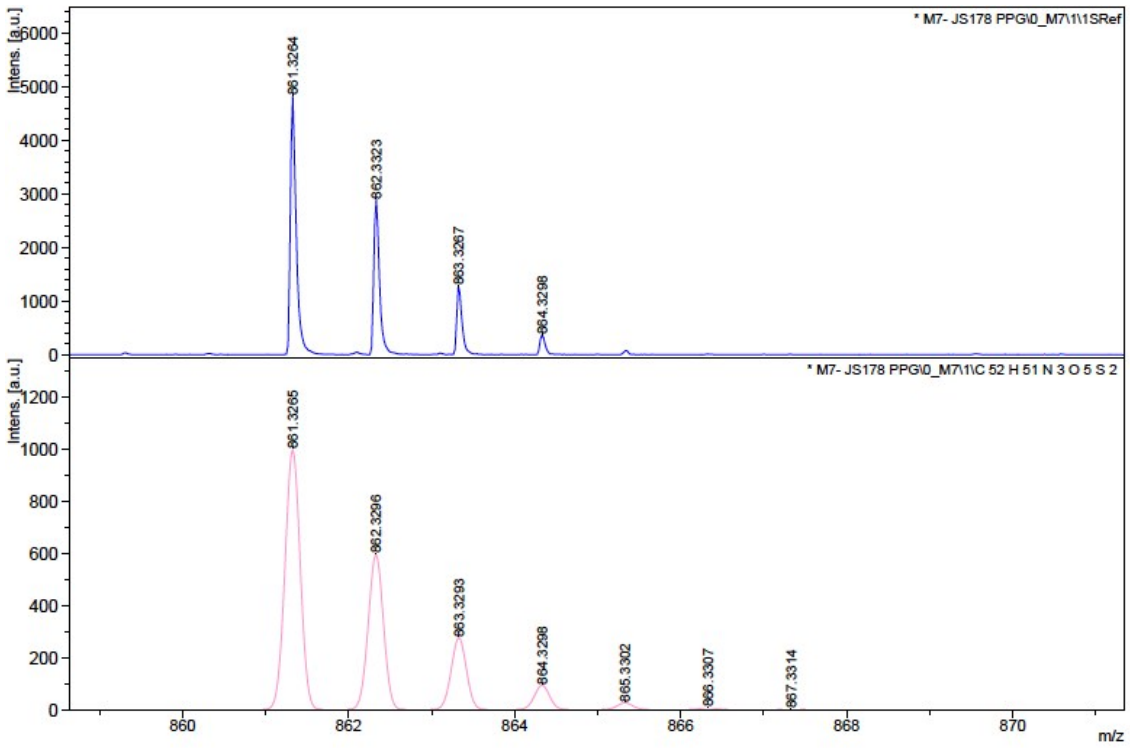

Figure S33. Recorded (top) and simulated (bottom) MALDI-TOF spectra of **M0**.

8. Device Fabrication and Characterization

Experimental devices had the following structure: Glass/ITO/PEDOT:PSS/Active layer/Ca/Al. ITO patterns were produced by photolithography of ITO-coated glass. 1/2 inch square cut pieces were washed in deionised water, acetone and isopropanol for 10 min, treated by oxygen plasma for 30 s, and coated by PEDOT:PSS (Heraeus Clevios Al4083) filtered through 0.45 µm PTFE. Inside a nitrogen-filled glovebox, the samples were spin-coated with the hot (90°C) preliminary stirred at least 12h at 70°C donor:PC70BM CB solution (D:A 1:3, 24 g/l total weight concentration). On the solar cells, Ca/Al (3/120 nm) layer was evaporated (0,2/1-2 Å/s) in a vacuum chamber (7 × 10-7 mbar). The solvent (CB) and thermal (130°C) annealing, as well as use of additives (1,8-diiodooctane, Chloronaphtalene) showed a limited effect on solar cell performance and thus were not applied to the presented samples. I-V characteristics have been measured under 1 sun simulated constant illumination (AM1.5G) in a nitrogen-filled chamber by source-measurement unit Keithley 2400.

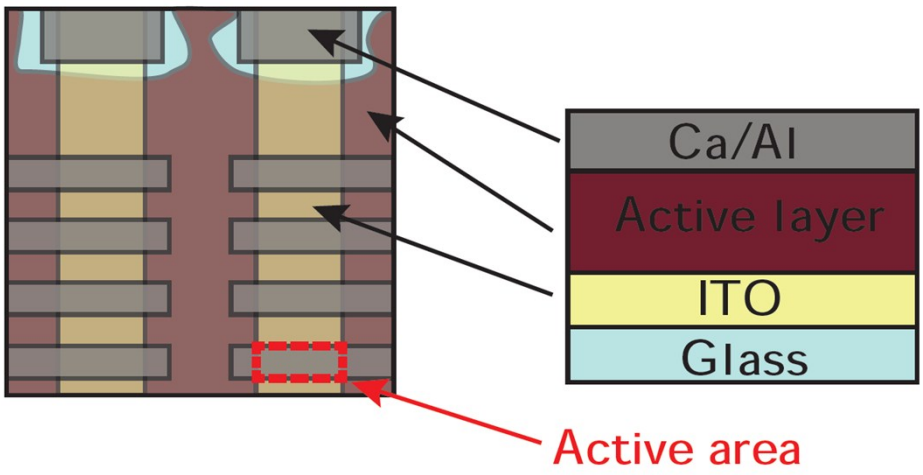

Figure S34. Solar cells device schematics.

9. Cation analysis

To investigate the species formed upon charge transfer from the donor rhodanine-based derivatives to the PCBM acceptor, theoretical calculations were performed on the singly positively-charged systems. Minimum-energy geometries were calculated for the singly-charged cations at the B3LYP/cc-pVDZ level of theory. Spin densities indicate that upon oxidation the electron is extracted mainly from the two TPA derivatives in the case of **M1**, **M3** and **M2**, whereas it also involves the fluorene–rhodanine core in **M0**.

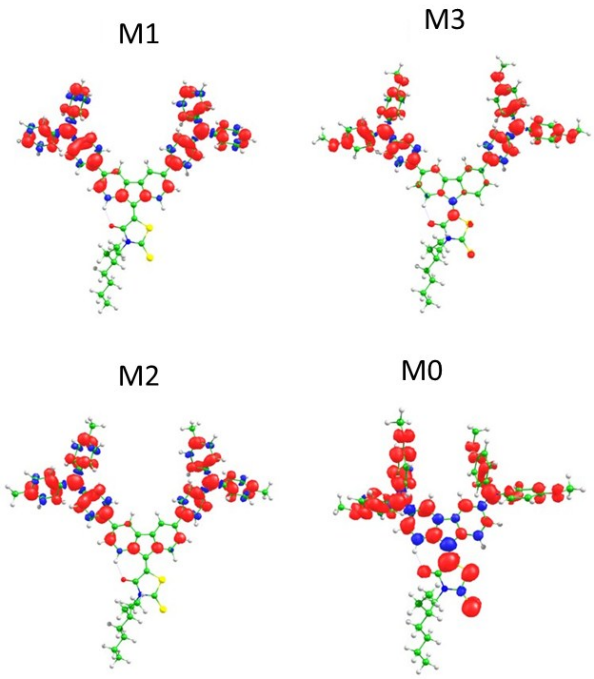

Figure S35. Spin densities (isovalue = 0.001) calculated for the cation species.

Reorganization energies (Λ) and first ionization potentials (IP) were calculated for the set of molecules according to the following expressions:

$$\Lambda = \lambda_1 + \lambda_2 = (E^{+1}_{N} - E^{+1}_{C}) + \left(E^{0}_{C} - E^{0}_{N}\right)$$

$$\mathrm{IP} = E^{+1}_{C} - E^{0}_{N}$$

where E^{Y}_{X} is the energy of the neutral (*Y* = 0) or the cation (*Y* = +1) species at the neutral (*X* = *N*) or the cation (*X* = *C*) geometry. Table 3 summarizes the values for these two magnitudes.

Table 3. Reorganization energy (Λ in kcal/mol) and ionization potential (IP in eV) calculated at the B3LYP/cc-pVDZ level of theory.

	Λ	IP
M0	3.13	5.768
M1	1.86	6.005
M2	1.60	5.834
M3	3.11	5.606

Since the oxidation takes place mainly in the donor TPA/DPA units, differences in the reorganization energy must be principally influenced by the peripheral substitutions. Indeed, **M0** and **M3** having –OMe moieties provide an identical reorganization energy of 3.1 kcal/mol (Table 3). Otherwise, **M1** is predicted with a Λ of 1.9 kcal/mol, whereas **M2** is calculated with the lowest reorganization energy of 1.6 kcal/mol. Looking now to the ionization potential, upon increasing the electron-donor character of the substituent going from **M1** (–H) to **M2** (–Me) and to **M3** (–OMe), the IP value decreases from 6.01 to 5.83 and to 5.61 eV, respectively (Table 3). The **M0** stands in between with an IP of 5.77 eV, which is larger than that of the analogously-substituted **M3** due to the direct linkage of the donor nitrogen atom to the fluorene–rhodanine acceptor core.

Time-dependent DFT calculations of the low-lying singlet excited states were performed on the cation species in order to assign the absorption features recorded in the femtosecond transition absorption experiments. We employed in this respect the long-range corrected LC-BLYP functional with the optimal γ value of 0.15 that nicely reproduced the position and intensity of both the CT and local excitations in our set of rhodanine-based derivatives.

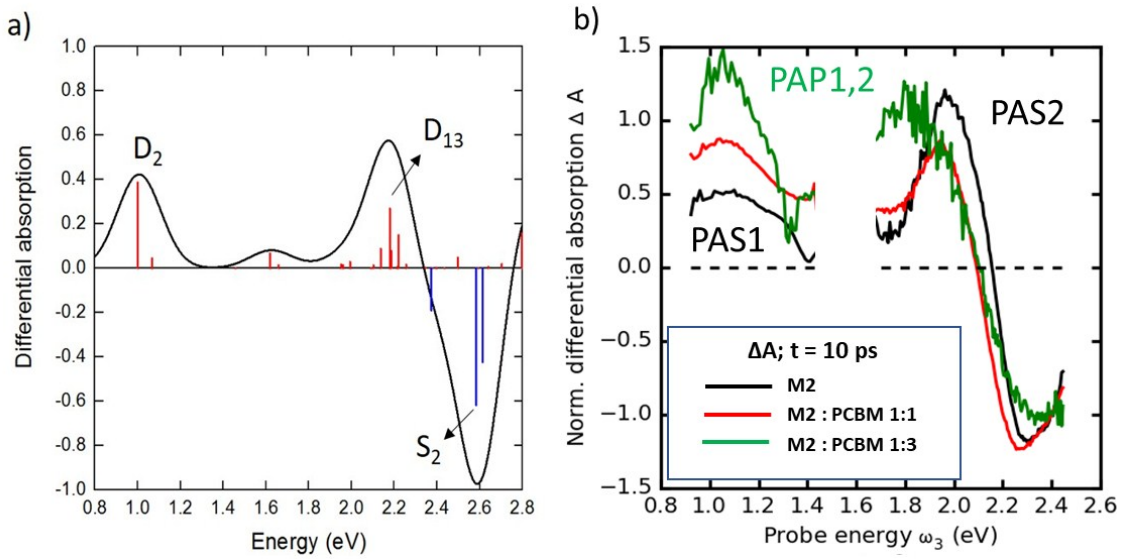

Figure S36. a) Differential absorption spectrum between the cation and the neutral species calculated at the LC-BLYP(0.15)/cc-pVDZ for the **M2**. Electronic excitations are depicted with vertical lines in red for the cation and in blue for the neutral species. S and D refer to singlet-to-singlet (for the netural) and doublet-to-doublet (for the cation) electronic excitations, respectively. b) Experimental femtosecond transient absorption (TA) spectra for **M2**.

Theoretical calculations predict two low-energy bands for the cation species of **M2** originated mainly from the electronic excitations D_2 and D_{13} with a CT nature (from Fl-Rh to TPA and vice versa, respectively). These two features are in very nice agreement with the two bands experimentally recorded in the TA experiments at c.a. 1.0 and 2.0 eV. Likewise, the TPA → Fl-Rh CT electronic transitions of the neutral species give rise to the bleaching experimentally recorded at 2.36 eV with a zero-crossing point at 2.2 eV, which is theoretically estimated in good accord at c.a. 2.3 eV.

10. References

1 Y. Song, W. Xu and D. Zhu, *Tetrahedron Lett.*, 2010, **51**, 4894−4897.

2 R. Anémian, D.C. Cupertino, P.R. Mackie and S.G. Yeates, *Tetrahedron Lett.*, 2005, **46**, 6717−6721.

3 K. Rakstys, A. Abate, M. I. Dar, P. Gao, V. Jankauskas, G. Jacopin , E. Kamarauskas, S. Kazim, S. Ahmad, M. Grätzel and M. K. Nazeeruddin, *J. Am. Chem. Soc.*, 2015, **137**, 16172−16178.

4 L. L. Hill, L. R. Moore, R. Huang, R. Craciun, A. J. Vincent, D. A. Dixon, J. Chou, C. J. Woltermann and K. H. Shaughnessy, *J. Org. Chem.*, 2006, **71**, 5117−5125.

5 R. Sandoval-Torrientes, J. Calbo, D. García-Fresnadillo, J. Santos, E. Ortí and N. Martín, *Org. Chem. Front*., 2017, **4**, 1024−1028.

6 a) C. Lee, W. Yang and R. G. Parr, *Phys. Rev. B*, 1988, **37**, 785−789; b) A. D. Becke, *J. Chem. Phys.*, 1993, **98**, 5648−5652.

7 T. H. Dunning Jr., *J. Chem. Phys.*, 1989, **90**, 1007−1023.

8 T. Etienne, X. Assfeld and A. Monari, *J. Chem. Theory Comput.*, 2014, **10**, 3896−3905.

9 T. Yanai, D. P. Tew and N. C. Handy, *Chem. Phys. Lett.*, 2004, **393**, 51.

10 T. Stein, L. Kronik and R. Baer, *J. Am. Chem. Soc.*, 2009, **131**, 2818.

11 a) R. Baer, E. Livshits and U. Salzner, *Annu. Rev. Phys. Chem.*, 2010, **61**, 85−109; b) B. M. Wong and T. H. Hsieh, *J. Chem. Theory Comput.*, 2010, **6**, 3704−3712; c) K. Okuno, Y. Shigeta, R. Kishi, H. Miyasaka and M. Nakano, *J. Photochem. Photobiol. A Chem.*, 2012, **235**, 29−34; d) K. Okuno, Y. Shigeta, R. Kishi and M. Nakano, *Chem. Phys. Lett.*, 2013, **585**, 201−206; e) J. Autschbach and M. Srebro, *Acc. Chem. Res.*, 2014, **47**, 2592−2602.

12 T. A. Reekie, M. Sekita, L. M. Urner, S. Bauroth, L. Ruhlmann, J.-P. Gisselbrecht, C. Boudon, N. Trapp, T. Clark, D. M. Guldi and F. Diederich, *Chem. Eur. J.*, 2017, **23**, 6357–6369.

13 V. Stokkum, Ivo HM, D. S. Larsen and R. van Grondelle, *BBA-BIOENERGETICS,* 2004, **1657**, 82–104.